






The largest plagiogranite on Earth formed by re-melting of juvenile proto-continental crust

Hamed Gamal El Dien ^{1,2✉}, Zheng-Xiang Li ^{1✉}, Mohamed Abu Anbar², Luc S. Doucet¹, J. Brendan Murphy ^{1,3}, Noreen. J. Evans ⁴, Xiao-Ping Xia ⁵ & Jiangyu Li¹

The growth of continental crust through melt extraction from the mantle is a critical component of the chemical evolution of the Earth and the development of plate tectonics. However, the mechanisms involved remain debated. Here, we conduct petrological and geochemical analyses on a large (up to 5000 km²) granitoid body in the Arabian-Nubian shield near El-Shadli, Egypt. We identify these rocks as the largest known plagiogranitic complex on Earth, which shares characteristics such as low potassium, high sodium and flat rare earth element chondrite-normalized patterns with spatially associated gabbroic rocks. The hafnium isotopic compositions of zircon indicate a juvenile source for the magma. However, low zircon $\delta^{18}\text{O}$ values suggest interaction with hydrothermal fluids. We propose that the El-Shadli plagiogranites were produced by extensive partial melting of juvenile, previously accreted oceanic crust and that this previously overlooked mechanism for the formation of plagiogranite is also responsible for the transformation of juvenile crust into a chemically stratified continental crust.

¹Earth Dynamics Research Group, The Institute for Geoscience Research (TIGeR), School of Earth and Planetary Sciences, Curtin University, Perth, WA, Australia. ²Geology Department, Faculty of Science, Tanta University, Tanta, Egypt. ³Department of Earth Sciences, St. Francis Xavier University, Antigonish, NS, Canada. ⁴John de Laeter Centre, School of Earth and Planetary Sciences, Curtin University, Perth, WA, Australia. ⁵State Key Laboratory of Isotope Geochemistry, Guangzhou Institute of Geochemistry, Chinese Academy of Sciences, Guangzhou, China. ✉email: hamed.gamaleldien@curtin.edu.au; z.li@curtin.edu.au

Deciphering the petrogenesis of granitic rocks has important implications for the understanding of the growth of continental crust¹. In contrast to widespread continental granitic rocks, plagiogranite is a rare leucocratic type predominantly composed of plagioclase (>40%), quartz, and ferromagnesian minerals (<10%, e.g., hornblende), with compositions ranging from diorite through trondhjemite to tonalite^{2,3}. Geochemically, they are characterized by very low K₂O (<1 wt. %), low Rb/Sr (<0.2 wt. %), high Na₂O (>3 wt. %), and flat rare-earth element (REE) chondrite-normalized patterns with enriched REE contents (10–100 times that of chondrite), distinguishing these trondhjemitic and tonalitic rocks from their continental equivalents^{2,3}.

In modern and ancient oceanic settings, plagiogranites mostly occur in mid-ocean ridge (MOR) settings and in ophiolite complexes^{4–10} where they are typically found as intrusions in gabbroic lower crust^{7,11} and/or lithospheric mantle (residual peridotite)^{5,12}. Two main competing, but not mutually exclusive, models have been proposed to explain their genesis: (1) late-stage fractional crystallization of basaltic magma at low pressures and (2) partial melting of pre-existing gabbroic oceanic crust. The first model implies that plagiogranites are highly differentiated felsic melts formed by the differentiation of parental MOR melt^{2,4}. The second model implies that plagiogranitic melts originate by partial melting of hydrothermally altered oceanic gabbros, triggered by the deep penetration of hydrothermal fluids into oceanic crust along shear zones/detachment faults^{11,13–17}.

Volumetrically, plagiogranites rarely exceed 1 vol. % of the oceanic crust, and range from dikes/veins a few millimeters to centimeters wide in MORs or ophiolites^{4,5,8}, to large granite bodies several hundred meters to kilometers in dimension, such as the Wadi Suhaylay plagiogranite in the Oman ophiolite that has surface dimensions of 10 km × 8 km^{6,7,14}. Until now, no plagiogranite larger than the Wadi Suhaylay plagiogranite has yet been reported. Here, we report the largest plagiogranitic complex (~5000 km²) discovered to date, located in the Eastern Desert of Egypt in the Arabian-Nubian Shield (ANS). We investigate the petrogenesis of this large plagiogranitic complex based on whole-rock geochemical and Sr-Nd isotopic data, as well as zircon U-Pb-Hf-O isotope and trace-element data. We then discuss its petrogenesis in the context of Neoproterozoic global-scale tectonics, which was dominated by Rodinia break-up.

The ANS is one of the largest exposures of Neoproterozoic juvenile continental crust on Earth (Fig. 1a)¹⁸, consisting of numerous terranes with widespread ophiolites¹⁹. Most previous studies proposed that crustal growth in the ANS occurred predominantly through arc accretion^{18,20}. Reymer and Schubert²¹ and Stein and Goldstein²² argued that the growth rate of the ANS significantly exceeded the rate of addition of mantle materials into the continental crust along modern subduction zones. They suggested that the large volume of magmas formed during the early stage of ANS crustal growth (within the Mozambique Ocean) may have been related to mantle plume magmatism (i.e., oceanic plateau). Gamal El Dien et al.²³ reported the occurrence of a voluminous ca. 700 Ma El-Shadli bimodal volcanic succession in the Eastern Desert region of the ANS, and speculated that a mantle plume may have provided sufficient heat to melt previously accreted oceanic terranes. In this work we adapt a similar plume model for the formation of the large plagiogranitic complex some 20–30 Myr prior to rift volcanism. We argue that contrary to conventional belief, the large plagiogranitic complex here formed through extensive re-melting of previously accreted oceanic crust driven by the emplacement of a mantle plume. Our work highlights the importance of mantle plumes in both the formation of exceptionally large plagiogranite intrusions, and in promoting crustal growth and consolidation in the ANS (and

possibly continental crust in general), through post-accretionary re-melting of accreted oceanic crust.

Results

Geology of the El-Shadli plutonic complex. The study area in the southern Eastern Desert region of Egypt consists of six major basement rock assemblages (Figs. 1b and 2). These assemblages include the Wadi Ghadir ophiolitic complex (Wadi, W, the Arabic word for ephemeral watercourses where many exposures occur), the El-Shadli granite-diorite-gabbro plutonic complex, the El-Shadli bimodal volcanic rocks, the W. Hafafit core complex, as well as post-collisional alkalic granites and volcanic rocks (collision here refers to the late Neoproterozoic continental collision related to the final assembly of Gondwana¹⁹) (Fig. 2).

The ca. 750 Ma W. Ghadir ophiolite assemblages (serpentinites, gabbroic rocks, sheeted dykes, and pillow basalts²⁴) are strongly deformed and variably metamorphosed²⁵. They have a dominantly NW-trending foliation that is truncated by the El-Shadli granitoids²⁶ (Fig. 2), consistent with the intrusive relationship documented in the northern part of the study area and indicating that the granitoids formed post regional terrane accretion. These granitoids are part of the El-Shadli granite-diorite-gabbro assemblage (the El-Shadli granitoids/plutonic complex) that crops out over much of the study area (Fig. 2). These granitoids have an almost continuous, arch-shaped map pattern in the central-south eastern part of the study region but are also exposed sporadically beneath the younger volcanic cover sequence (the El-Shadli bimodal volcanics), suggesting the possibility of a large and continuous plutonic complex underlying much of the region (Fig. 2). The estimated dimension of such a plutonic complex is ca. ~100 km × 50 km.

The El-Shadli volcanic rocks are the largest bimodal suite exposed (80 km × 35 km), not only in the Eastern Desert of Egypt but also in the ANS^{23,27}. They occur in a WNW-ESE trending belt flanked by granite-diorite-gabbro rocks (Fig. 2). The mafic endmember of the bimodal volcanic rocks consists of massive to pillow basaltic lava flows and dike swarms that intrude the granitoid rocks (Supplementary Fig. 1a). The felsic endmember consists of massive rhyolitic lava flows. The El-Shadli bimodal volcanic rocks had an imprecise Rb-Sr isochron age of ~710 ± 24 Ma²⁷. A recent study²³ provided a precise U-Pb zircon age of ~700 Ma, and concluded that the El-Shadli bimodal volcanic rocks were generated in a post-accretionary rift-related environment²⁷, possibly induced by a mantle plume²³.

The 680–630 Ma W. Hafafit Core complex is exposed in the NW part of the study area and is composed mainly of granitoids, gneisses, and amphibolites²⁸ (Fig. 2). The post-collisional alkaline granites (~640–550 Ma) are located in the eastern part of the study area and intrude both the El-Shadli plutonic complex and bimodal volcanics^{29,30} (Fig. 2). Post-collisional alkaline volcanic rocks and their pyroclastic equivalents occur around W. Ranga (W. Ranga volcanics) in the eastern part of the study area (Fig. 2). This sequence comprises two slightly metamorphosed volcanic sequences: (a) intermediate-mafic lava flows (andesites, basaltic andesites, and basalts) in the north near Gabal (G) El-Sarobi and (b) felsic rocks (rhyolitic and dacitic lava flows) in the south. Previously undated, these volcanic rocks were interpreted to reflect either a post-collisional setting³⁰ or pre-collisional intra-oceanic arc assemblage²⁹. In addition, previous work^{29,30} inferred that the W. Ranga volcanic rocks were intruded by the El-Shadli granite-diorite-gabbro assemblage, although contact relationships are unclear in the field. However, these interpretations are not supported by a new zircon U/Pb age of 585 ± 10 Ma³¹, which indicates that the volcanic rocks are significantly younger than the El-Shadli granite-diorite-gabbro assemblage (see below).

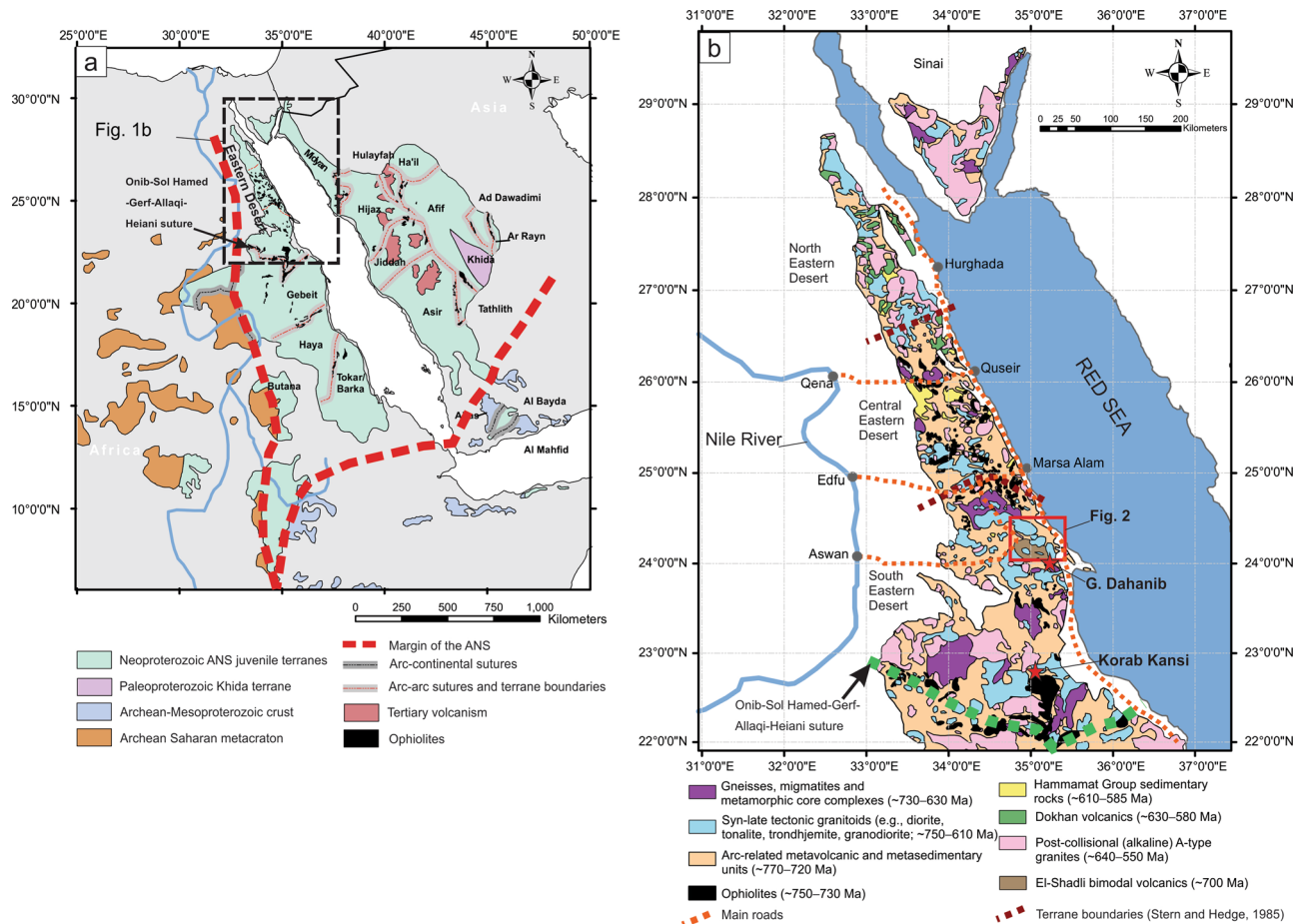


Fig. 1 Geological map of the Arabian-Nubian Shield, including the Eastern Desert²³. **a** A schematic geological map of the Arabian-Nubian Shield (ANS) with location of the study region (modified after Johnson et al.¹⁹). **b** A simplified geological map of the Eastern Desert showing the major Neoproterozoic basement rocks^{19,23}. Terrane boundaries follow that of Stern and Hedge⁹⁷.

Sample description and petrography. The El-Shadli granitoids occur as massive plutons. Within individual batholiths, 1 × 1 to 5 × 2 m gabbroic diorite enclaves represent over 50% of the outcrop area and provide evidence of extensive magmatic mixing zones (Fig. 3a, a-I and Supplementary Fig. 1b). The enclaves show no obvious chilled margins and have irregular, scalloped contacts with the granite (Fig. 3a-I). A similar magmatic mixing zone has been described in the Oman ophiolite plagiogranitic suite⁶. Smaller (centimeter-sized) ultramafic/mafic enclaves occur within the studied gabbroic diorite rocks and granites (Fig. 3b-d).

The El-Shadli samples include tonalites, trondhjemites, diorite, and gabbro (Fig. 3 and Supplementary Fig. 1c-e), a typical rock association in ophiolitic plagiogranite suites^{3,5-8,10}. The granite samples range from fine- to coarse-grained hypidiomorphic-granular rocks, consisting of zoned plagioclase (50–55%), quartz (35–40%), and hornblende <5% (Fig. 3e, f-I and Supplementary Fig. 2). Quartz-plagioclase intergrowths such as graphic and vermicular textures, typical of plagiogranites³, are observed in the studied granites (Fig. 3f-I and Supplementary Fig. 3a, b). Fe-Ti oxides, zircon, titanite, and apatite are common accessory minerals (Fig. 3e, f-I and Supplementary Fig. 2). Actinolite, sericite, clay minerals, and chlorite are the main secondary minerals. Detailed petrographic descriptions and modal compositions for all the studied samples are provided in the Supplementary information.

Whole-rock geochemical data. Petrographic observations indicate that the El-Shadli granitoid samples are fresh with very minor

visible evidence of secondary alteration. These observations are consistent with the low loss on ignition (LOI) values (typically less than 1.2 wt. %, Supplementary Data 1) and indicate that the samples experienced no significant alteration that would affect the abundances of petrogenetic-indicating high field strength elements and REE. The compositional range of the El-Shadli granitic (including dioritic) samples is: SiO₂ (60.3–78.5 wt. %), Al₂O₃ (11.8–15.5 wt. %), Fe₂O₃^T (1.3–10.9 wt. %), TiO₂ (0.1–1.4 wt. %), and MgO (0.1–1.7 wt. %) (Supplementary Fig. 5 and Supplementary Data 1). This geochemistry differs from the felsic end-member of the overlying El-Shadli bimodal volcanics²³, which is characterized slightly higher silica content (>75 wt. %: Fig. 4b) and lower Fe₂O₃^T (<3.5 wt. %), TiO₂ (0.3 wt. %), and MgO (0.6 wt. %), but a similar range in Al₂O₃ (11.3–13.2 wt. %). The El-Shadli granitoids have ferroan characteristics with Fe-number [FeO^T / (FeO^T + MgO)] ranging between 0.72 and 0.91 (Supplementary Fig. 5a) and have a calcic affinity according to the modified alkali-lime index (MALI = Na₂O + K₂O - CaO) (Supplementary Fig. 5b)³².

Gabbroic samples S11-1 and S12 have a composition of SiO₂ = 45.8–47.5 wt. %, Al₂O₃ = 15.6–18.5 wt. %, Fe₂O₃^T = 8.6–12.2 wt. %, TiO₂ = 0.8–1.4 wt. %, and MgO = 7.9–15.6 wt. % (Supplementary Fig. 4 and Supplementary Data 1). These major element concentrations are very similar to the mafic endmember of the overlying El-Shadli bimodal volcanics, except for the lower MgO (4.2–9.2 wt. %) in the latter²³. All the analyzed samples have very low K₂O (<1 wt. %) and total alkali contents (K₂O + Na₂O = 4.0–6.5 wt. %) (Fig. 4 and Supplementary Data 1).

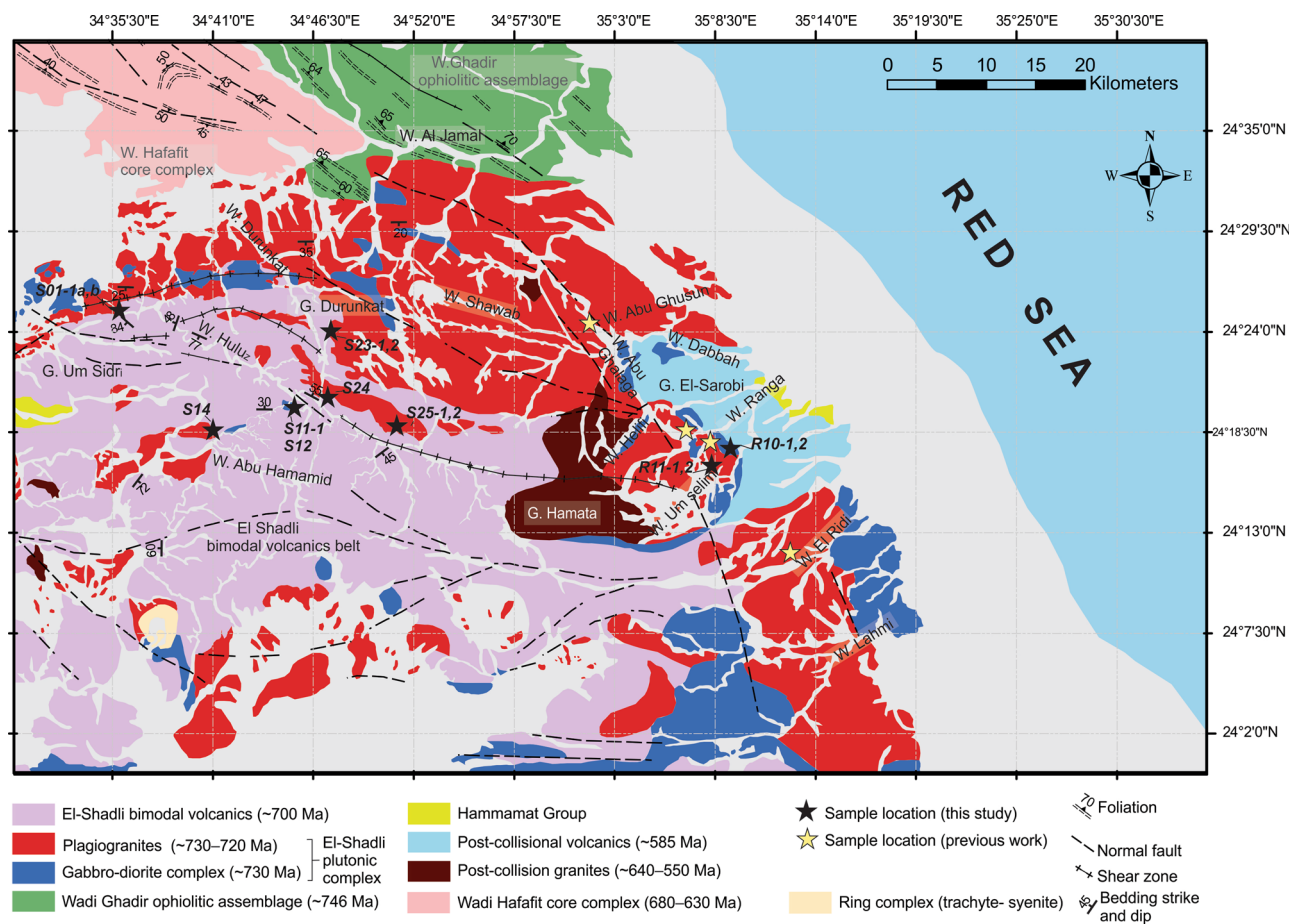


Fig. 2 Geological map of the studied El-Shadli area with sample locations (after Gamal El Dien et al.²³ and Jabal Hamatah quadrangle⁹⁸). The rock units include the El-Shadli bimodal volcanic rocks, the El-Shadli plagiogranites-diorite-gabbro assemblage (this study), the W. Ghadir ophiolitic assemblage, the W. Hafafit core complex, post-collision alkaline granites, and post-collisional volcanics. Age data are from Kroner et al.²⁵, Stern et al.²⁷, Gamal El Dien et al.²³, Kroner et al.²⁸, Gamal El Dien³¹, and this study.

In general, the studied samples show a distinctive flat REE pattern with slight LREE depletion, similar to that of the overlying El-Shadli bimodal volcanics²³ (Fig. 5a). The El-Shadli granites (including diorite samples) show similar MORB-like REE patterns with 5–40 times enrichment relative to chondrite³³, and slightly negative Eu anomalies [$(Eu/Eu^*)_{CI} = 0.28-0.95$] (Fig. 5a). The associated gabbroic rocks mimic and completely overlap the REE pattern [$(La/Sm)_{CI} < 0.47$ and $(Yb/Gd)_{CI} < 0.84$] of the granitic rocks [$(La/Sm)_{CI} = 0.56-1.22$ and $(Yb/Gd)_{CI} = 0.71-1.29$] (Fig. 5a). On the N-MORB-normalized trace-element diagram³⁴ (Supplementary Fig. 6a), all samples exhibit flat MORB-like patterns, except for some with negative Ti and Nb anomalies and slightly positive Pb anomalies. Large ion lithophile elements (LILE) such as Cs, Rb, Ba, Th, and U show some enrichment relative to N-MORB³⁴.

Whole-rock Sr-Nd isotope data. All the studied samples have low concentrations of Sr (43.29–207.92 ppm) and Rb (1.03–13.45 ppm), and $^{87}Sr/^{86}Sr$ ratios ranging between 0.702637 ± 0.000002 and 0.708406 ± 0.000007 (Supplementary Data 1). They also have low Nd (4.42–26.61 ppm) and Sm (1.60–8.65 ppm) with measured $^{143}Nd/^{144}Nd$ ratios of 0.512871 ± 0.000001 to 0.513165 ± 0.000012 (Supplementary Data 1). The calculated initial $^{87}Sr/^{86}Sr$ ratios range from 0.702027 to 0.703401, and the initial $^{143}Nd/^{144}Nd$ ratios from 0.511973 to 0.512111 (Supplementary Fig. 7 and Supplementary Data 1). The calculated $\epsilon Nd(t)$ values range from +5.55 to +8.18 (Supplementary Fig. 7), similar to those of the El-Shadli bimodal

volcanics²³, with the corresponding T_{DM} model ages^{35,36} ranging from 0.78 to 1.2 Ga.

Zircon U-Pb-Hf-O isotopes and trace elements

Diorite sample R10-1. Zircon grains from sample R10-1 have equant to sub-rounded morphologies and range from 100–>200 μm in length (Fig. 6a and Supplementary Fig. 8a). In cathodoluminescence (CL) images, some zircon grains display relatively subhedral to euhedral rims with clear concentric oscillatory zoning (Fig. 6a and Supplementary Fig. 8a), but the majority have anhedral corroded rims with oscillatory, convolute, or convoluted/mottled zoning patterns (Fig. 6a and Supplementary Fig. 8a). We carefully excluded from our analysis those grains with either mottled or convoluted zones. For sample R10-1, 14 U-Pb Sensitive High-Resolution Ion Microprobe (SHRIMP) analyses conducted on 14 grains yielded variable U (142–680 ppm) and Th (69–1310 ppm) contents and high Th/U ratios (0.48–4.42) (Supplementary Data 2). The high Th/U ratios are typical of zircons crystallized from low SiO_2 melts (i.e., gabbro-diorite rocks)³⁷. The U-Pb isotopic analyses yield a weighted mean $^{206}Pb/^{238}U$ age of 733 ± 7 Ma ($\pm 95\%$ conf., mean square of weighted deviates [MSWD] = 0.76, $N = 13$; Fig. 6a), which is interpreted as the crystallization age of the gabbro-diorite complex. Eighteen laser ablation split stream (LASS) analyses on the same sample were conducted on 18 grains, including analyses over the same 14 spots utilized for SHRIMP analyses. The LASS analyses yield a similar $^{206}Pb/^{238}U$ age of 732 ± 5 Ma ($\pm 95\%$ conf., MSWD = 1.4, $N = 18$; Supplementary Fig. 9a). Chondrite (CI)-normalized³³ REE patterns of the zircons exhibit a negative slope

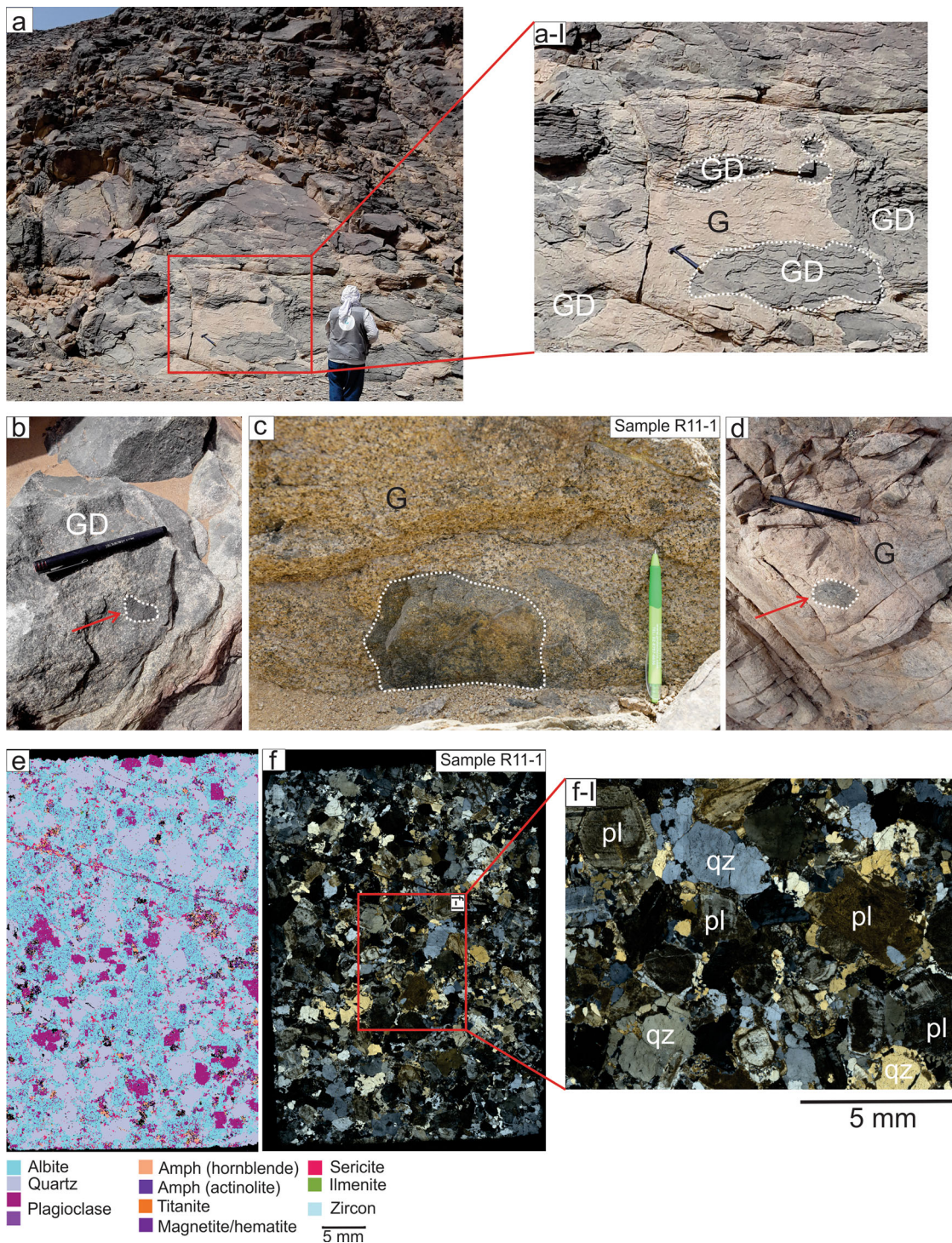


Fig. 3 Field photos and photomicrographs of the El-Shadli plagiogranites and associated gabbros. **a, a-l** Magmatic mixing zone between the plagiogranites and associated gabbroic dioritic rocks. The large mafic enclaves in the mixing zone show no obvious chilled margin and have irregular boundaries with the plagiogranites. **b-d** Centimeter-size mafic enclaves within gabbroic diorites and plagiogranites. **e** TIMA map showing the distribution of the minerals in the sample R11-1. **f, f-l** Crossed-polarized light images of the sample R11-1 showing coarse-grained hypidiomorphic-granular texture and quartz-plagioclase intergrowths such as graphic and vermicular textures. The rock consists mainly of plagioclase (pl) and quartz (qz). GD = Gabbro-diorite rocks, G = Plagiogranites.

from middle to heavy REE with $(Yb/Gd)_{CI} = 29-42$, and subdued negative Eu anomalies $[(Eu/Eu^*)_{CI} = 0.13-0.28]$, a feature that is typical of unaltered magmatic zircons³⁸ (Supplementary Fig. 9a). Zircon grains have variable Hf contents (7843–10,390 ppm), Nb contents (0.59–2.46 ppm), and U/Yb ratios (0.06–0.23) (Fig. 7a, b, Supplementary Fig. 10a, and Supplementary Data 3). The Lu-Hf

isotopic analyses of these 18 spots yield $^{176}Lu/^{177}Hf$ ratios of 0.004320 ± 0.000340 to 0.008358 ± 0.000099 and $^{176}Hf/^{177}Hf(t_0)$ ratios of 0.282596 ± 0.000064 to 0.282760 ± 0.000077 (Supplementary Data 3). Calculated $\epsilon Hf(t_0)$ values range from $+9.70 \pm 0.96$ to $+13.43 \pm 1.16$, with a weighted mean of $+11.56 \pm 0.51$ (MSWD = 1.12) (Fig. 7c, d, Supplementary Fig. 10b, and Supplementary Data 3), corresponding

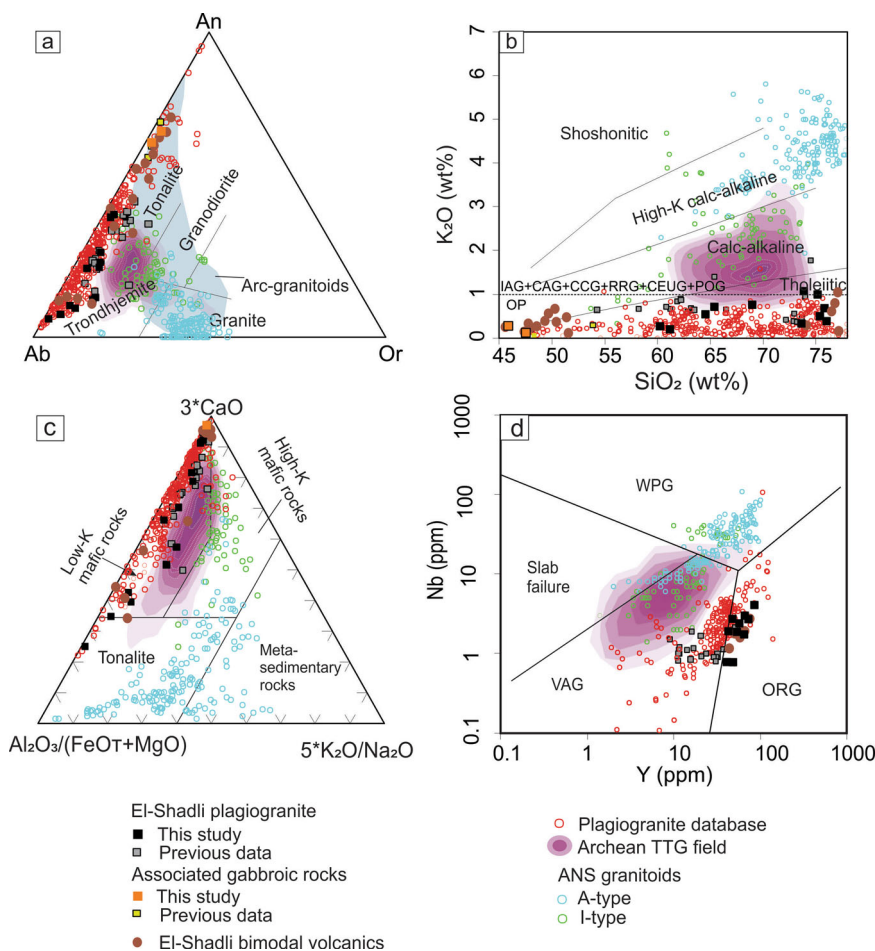


Fig. 4 Geochemical and tectonic classification diagrams. **a** Ab-An-Or diagram^{41,42}. **b** SiO_2 (wt%) vs. K_2O (wt%) plot⁹⁹. Fields for oceanic plagiogranites (OP), island arc granitoids (IAG), continental arc granitoids (CAG), continental collision granitoids (CCG), post-orogenic granitoids (POG), rift-related granitoids (RRG), and continental epeirogenic uplift granitoids (CEUG) are after Maniar et al.¹⁰⁰. **c** Ternary diagram of $\text{Al}_2\text{O}_3/(\text{FeOT} + \text{MgO})-3^*\text{CaO}-5^*(\text{K}_2\text{O}/\text{Na}_2\text{O})$ ⁴³ showing that the studied plagiogranites were likely derived from a low-K mafic magma source. **d** Tectonic setting plot⁴⁰. Data sources: previously reported plagiogranites are as referenced in the text; arc granitoids (gray shade in **a**) are extracted from open access GeoRoc repository¹⁰¹; Archean trondhjemite-tonalite-granodiorite (TTG; purple shades)⁴⁷; other ANS I- and A-type granitoids^{44,45}; the EI-Shadli bimodal volcanics²³.

with two-stage Hf model ages (T_{DM} crustal) of 0.77–1.02 Ga. Although spot R10-1-15 has $\epsilon\text{Hf}(t) = 15.21 \pm 1.16$ and $T_{\text{DM}} = 0.66$ Ga, the young T_{DM} age of this spot compared to the crystallization age of the sample suggests recent Pb loss. As a result, the data from this spot were not included in the $\epsilon\text{Hf}(t)$ weighted mean calculations. The T_{DM} crustal calculation assumes a $^{176}\text{Lu}/^{177}\text{Hf}$ value of 0.015, an average value for the continental crust³⁹. The same 18 spots were also analyzed by secondary ion mass spectrometry (SIMS) for O isotopic data, and yield $\delta^{18}\text{O}$ values in the range of 4.33 ± 0.29 to 5.09 ± 0.24 ‰ with a weighted mean of 4.73 ± 0.1 ‰ (MSWD = 1.09) (Fig. 7d, Supplementary Figs 10c and 11, and Supplementary Data 3).

Trondhjemite sample R11-1. Zircon grains from sample R11-1 are commonly >200 μm in length and are equant to prismatic with euhedral rims. These grains show homogenous textures, some with well-developed oscillatory zoning in CL images, but others with faint and broad zoning (Fig. 6b and Supplementary Fig. 8). Sixteen U-Pb SHRIMP analyses on 16 grains yielded variable U (135–1241 ppm) and Th (53–703 ppm) contents, and Th/U ratios of 0.37–0.66 (Supplementary Data 2), typical of zircons that crystallized in a high- SiO_2 magma³⁷. The 16 analyses form a tight cluster that yields a weighted mean $^{206}\text{Pb}/^{238}\text{U}$ age of 733 ± 3 Ma ($\pm 95\%$ conf., MSWD = 0.11, $N = 16$; Fig. 6b), interpreted to be the crystallization age of the

Trondhjemite. Thirty-eight LASS analyses of 38 grains included 16 grains that were analyzed by SHRIMP, usually over the same spots. Taken together, these LASS analyses yield a $^{206}\text{Pb}/^{238}\text{U}$ age of 730 ± 3 Ma ($\pm 95\%$ conf., MSWD = 0.87; Supplementary Fig. 9b and Supplementary Data 3) that is within analytical uncertainty of the SHRIMP age. CI-normalized³³ zircon REE patterns are similar to those of sample R10-1 and are characterized by a negative slope from the middle to heavy REE [$(\text{Yb}/\text{Gd})_{\text{CI}} = 15\text{--}28$]. They are also characterized by negative Eu anomalies [$(\text{Eu}/\text{Eu}^*)_{\text{CI}} = 0.06\text{--}0.12$], typical of unaltered magmatic zircons³⁸ (Supplementary Fig. 9b and Supplementary Data 3), and by high Hf (7873–13,098 ppm), low Nb (1.01–17.8 ppm), and U/Yb ratios ranging from 0.06 to 0.22 (Fig. 7a, b, Supplementary Fig. 10a, and Supplementary Data 3). The Lu-Hf isotopic analyses of these 38 spots yield $^{176}\text{Lu}/^{177}\text{Hf}$ ratios ranging from 0.00272 ± 0.00011 to 0.01162 ± 0.00020 and $^{176}\text{Hf}/^{177}\text{Hf}(t)$ ratios from 0.282570 ± 0.000086 to 0.282710 ± 0.0000680 (Supplementary Data 3). Calculated $\epsilon\text{Hf}(t)$ values range from $+8.66 \pm 1.01$ to $+13.39 \pm 0.80$ and have a weighted mean of $+10.82 \pm 0.17$ (MSWD = 1.01) (Fig. 7c, d, Supplementary Fig. 10b, and Supplementary Data 3), corresponding with T_{DM} crustal formation ages of 0.77–1.07 Ga. Twenty O isotope analyses of these zircons yield $\delta^{18}\text{O}$ values ranging from 4.38 ± 0.15 ‰ to 4.88 ± 0.16 ‰ with a weighted mean of 4.57 ± 0.04 ‰ (MSWD = 0.51) (Fig. 7d, Supplementary Figs 10c and 11, and Supplementary Data 3).

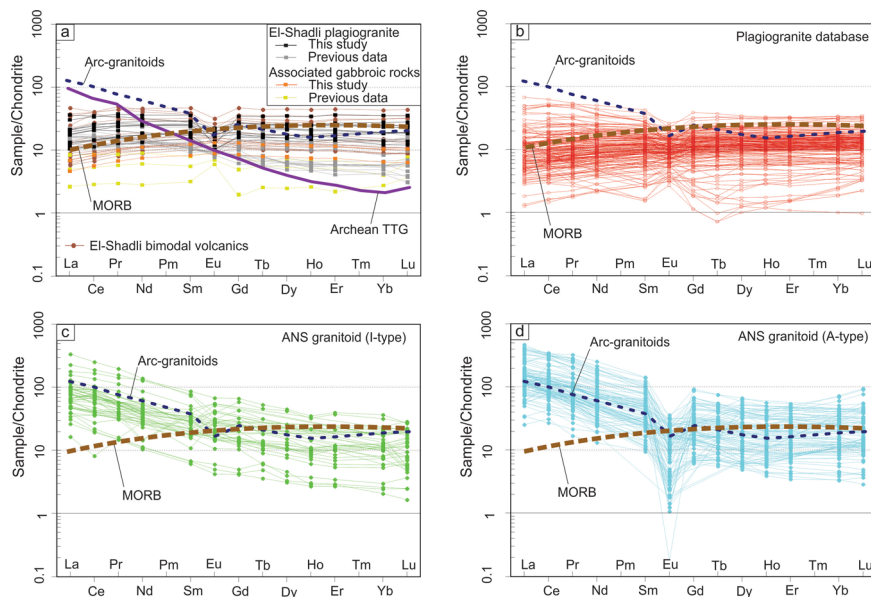


Fig. 5 Chondrite-normalized rare-earth element patterns of the El-Shadli plagiogranites and associated gabbros, other Arabian-Nubian Shield granitoids, and known global plagiogranites plotted against that of global MORB and arc granitoids trends. **a** REE patterns of the El-Shadli plagiogranites and associated gabbros compared to that of global MORB (brown dashed line)³⁴, arc granitoids (blue dashed line; data are extracted from open access GeoRoc repository)¹⁰¹, Archean TTG (purple solid line)⁴⁷, and the El-Shadli bimodal volcanics²³. **b** Global plagiogranite database compared to that of MORB and arc granitoids. **c, d** Other ANS granitoids data^{44,45} compared to that of global MORB and arc granitoids: I-type granitoids (**c**) and A-type granitoids (**d**).

Trondhjemite sample S01-1a. Zircon grains from sample S01-1a are euhedral with lengths <200 μm . Most grains exhibit well-developed concentric oscillatory zoning, although some have homogenous cores (Fig. 6c and Supplementary Fig. 8). Twenty U-Pb SHRIMP analyses on 19 grains yielded relatively low U (28–153 ppm) and Th (13–257 ppm) contents, and Th/U ratios of 0.38–0.65 (Supplementary Data 2) that are indicative of a magmatic origin. Spot #S01-1-2 has a high common ^{206}Pb (6.9%), and this analysis is not included in the age calculation. The remaining 19 analyses yield a weighted mean $^{206}\text{Pb}/^{238}\text{U}$ age of 729 ± 7 Ma ($\pm 95\%$ conf., MSWD = 0.37, $N = 19$; Fig. 6c), which is interpreted as the crystallization age of this Trondhjemite sample. Thirty LASS analyses were conducted on 30 grains, with 20 analyses from the same spots as the SHRIMP analyses, usually over the SHRIMP spot. These analyses yield a $^{206}\text{Pb}/^{238}\text{U}$ age of 728 ± 4 Ma ($\pm 95\%$ conf., MSWD = 0.69, $N = 27$; Supplementary Fig. 9c and Supplementary Data 3), which overlaps (within uncertainty) with the SHRIMP age. CL-normalized³³ zircon REE patterns show negative middle to heavy REE slopes $[(\text{Yb}/\text{Gd})_{\text{CI}} = 10\text{--}41]$, as well as anomalies in Eu $[(\text{Eu}/\text{Eu}^*)_{\text{CI}} = 0.06\text{--}0.12]$ and Ce $[(\text{Ce}/\text{Ce}^*)_{\text{CI}} = 0.4\text{--}16; \text{Ce}^* = \sqrt{(\text{La} \times \text{Pr})}]$. Such features are typical of magmatic zircons³⁸ (Supplementary Fig. 9c and Supplementary Data 3). The zircon grains have Hf contents ranging from 8182 to 9859 ppm, Nb from 0.73 to 3.06 ppm, and U/Yb ratios from 0.04 to 0.12 (Fig. 7a, b, Supplementary Fig. 10a, and Supplementary Data 3). The Lu-Hf isotopes of these 30 spots yield $^{176}\text{Lu}/^{177}\text{Hf}$ ratios ranging from 0.001548 ± 0.00002 to 0.00668 ± 0.00020 and $^{176}\text{Hf}/^{177}\text{Hf}_{(\text{t})}$ ratios from 0.282566 ± 0.000038 to 0.282725 ± 0.000043 (Supplementary Data 3). The calculated $\epsilon\text{Hf}_{(\text{t})}$ values range from $+8.51 \pm 0.59$ to $+14.40 \pm 0.83$ with a weighted mean of $+11.00 \pm 0.12$ (MSWD = 4.3) (Fig. 7c, d, Supplementary Fig. 10b, and Supplementary Data 3), which corresponds with T_{DM} crustal formation ages of 0.72–1.09 Ga. Twenty O isotope spot analyses yield $\delta^{18}\text{O}$ values ranging between $4.32 \pm 0.24\text{‰}$ and $5.09 \pm 0.20\text{‰}$ with a weighted mean of $4.83 \pm 0.09\text{‰}$ (MSWD = 0.97) (Fig. 7d, Supplementary Figs 10c and 11, and Supplementary Data 3).

Trondhjemite sample S14. Zircon grains from sample S14 are equant to sub-rounded, with euhedral rims. They range in length from 50 to 150 μm . Zircon grains commonly show oscillatory zoning in CL images, although some display homogenous cores (Fig. 6d and Supplementary Fig. 8). Nineteen U-Pb SHRIMP analyses conducted on 19 grains yield U and Th contents of 48–937 and 20–1451 ppm, respectively, with Th/U ratios ranging from 0.31 to 1.55 (Supplementary Data 2). These values are consistent with a magmatic origin. Seventeen of the 19 U-Pb isotopic analyses yield a weighted mean $^{206}\text{Pb}/^{238}\text{U}$ age of 722 ± 7 Ma ($\pm 95\%$ conf., MSWD = 0.41, $N = 17$; Fig. 6d), which is interpreted as the crystallization age of the sample. Nineteen LASS analyses located over the same 19 SHRIMP spots yield a $^{206}\text{Pb}/^{238}\text{U}$ age of 722 ± 11 Ma ($\pm 95\%$ conf., MSWD = 3.5, $N = 19$; Supplementary Fig. 9d and Supplementary Data 3), which is identical within error to the SHRIMP age. All zircons have REE patterns characterized by negative slopes $[(\text{Yb}/\text{Gd})_{\text{CI}} = 14\text{--}29]$, negative Eu anomalies $[(\text{Eu}/\text{Eu}^*)_{\text{CI}} = 0.12\text{--}0.52]$, but highly variable Ce anomalies $[(\text{Ce}/\text{Ce}^*)_{\text{CI}} = 1.06\text{--}114]$, characteristics typical of magmatic zircons³⁸ (Supplementary Fig. 9d and Supplementary Data 3). Zircon grains have Hf concentrations ranging from 8515 to 11,322 ppm, Nb from 0.80 to 9.37 ppm, and U/Yb ratios from 0.07 to 0.47 (Fig. 7a, b, Supplementary Fig. 10a, and Supplementary Data 3). Lu-Hf isotopic analyses of the same 19 spots give $^{176}\text{Lu}/^{177}\text{Hf}$ ratios of 0.000936 ± 0.000009 to 0.011387 ± 0.000083 and $^{176}\text{Hf}/^{177}\text{Hf}_{(\text{t})}$ ratios of 0.282577 ± 0.000041 to 0.282724 ± 0.000045 (Supplementary Data 3). Calculated $\epsilon\text{Hf}_{(\text{t})}$ values range from $+9.39 \pm 0.62$ to $+13.19 \pm 1.08$ and give a weighted mean of $+11.38 \pm 0.56$ (MSWD = 3.3) (Fig. 7c, d, Supplementary Fig. 10b, and Supplementary Data 3), corresponding to T_{DM} crustal formation ages of 0.78–1.05 Ga. These 19 spots have $\delta^{18}\text{O}$ values of $4.06 \pm 0.17\text{--}4.93 \pm 0.25\text{‰}$ with a weighted mean of $4.52 \pm 0.14\text{‰}$ (MSWD = 2.4) (Fig. 7d, Supplementary Figs 10c and 11, and Supplementary Data 3).

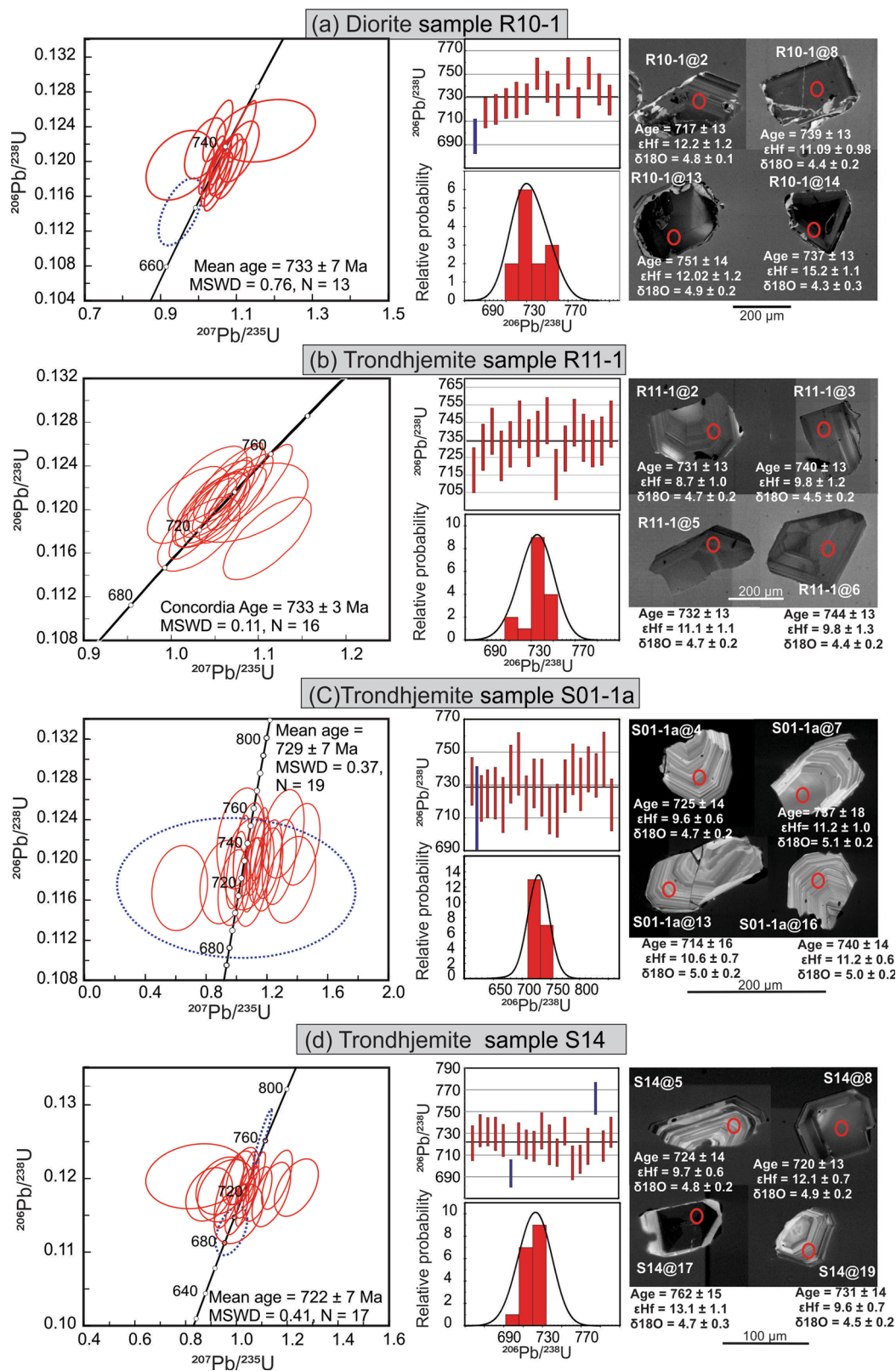


Fig. 6 Geochronological data and cathodoluminescence images of the El-Shadli plagiogranites. a–d Zircon U–Pb SHRIMP Concordia diagrams show the $^{206}\text{Pb}/^{238}\text{U}$ ages of the analyzed zircons with 2 sigma errors for samples R10-1 (**a**), R11-1 (**b**), S01-1a (**c**), and S14 (**d**). Weight means and relative probability diagrams of $^{206}\text{Pb}/^{238}\text{U}$ age, and representative cathodoluminescence (CL) images, are shown for each sample. The red ovals on the CL images mark the spots for SHRIMP, LASS, and SIMS analyses for the U–Pb age, Hf and O isotopes, and trace-element data, respectively.

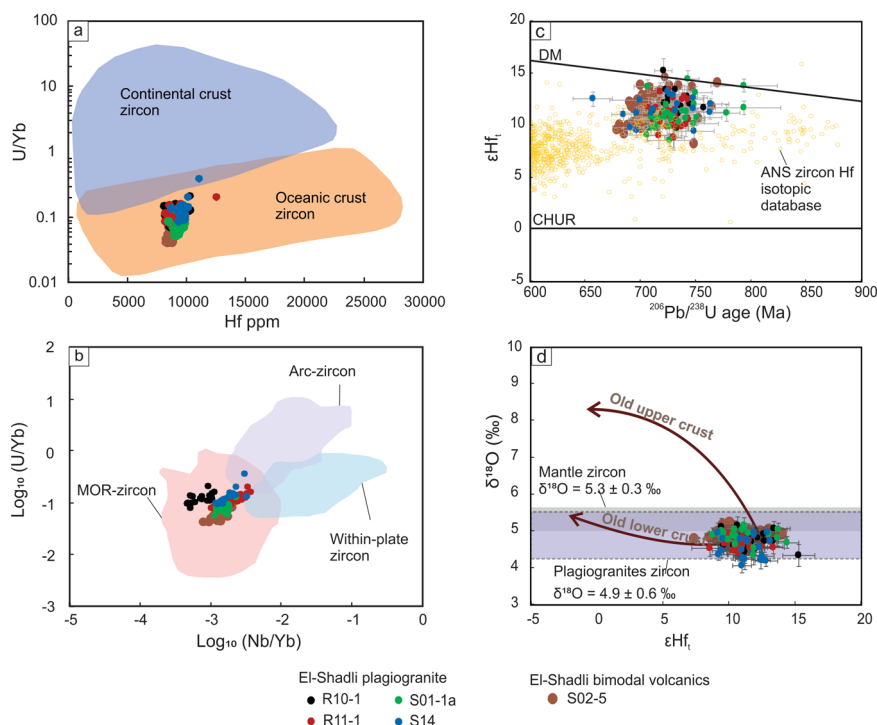


Fig. 7 Trace elements, age, hafnium, and oxygen isotopic data of zircons from the El-Shadli plagiogranites. **a, b** Zircon trace elements tectono-magmatic classification plot³⁸ of the El-Shadli plagiogranites. The fields for continental crust and oceanic crust zircons and from Grimes et al.³⁸ **c** ϵHf_t vs. $^{206}\text{Pb}/^{238}\text{U}$ age plot against the Chondritic uniform reservoir (CHUR) and depleted mantle (DM) lines³⁹. Hf isotopic data of ANS arc-related I- and A-type granitoids (yellow circles)⁴⁴ are used for comparison. **d** The plot of $\delta^{18}\text{O}$ (‰) vs. ϵHf_t for the studied zircons. Old upper and lower crust trends are from Wang et al.⁹ The zircon $\delta^{18}\text{O}$ value of oceanic ophiolitic plagiogranites is $4.9 \pm 0.6\text{‰}$ ⁷ (purple shadow) and that of mantle zircons is $5.3 \pm 0.3\text{‰}$ ⁴⁶ (gray shadow). Data for the El-Shadli bimodal volcanics are from Gamal El Dien et al.²³. Error bars represent 2 sigma.

Discussion

El-Shadli plagiogranites: mineralogical, petrological, and geochemical evidence. Plagiogranites are distinguished from other granite types based on mineralogical and geochemical criteria^{2,3,40}. The modal mineralogy (plagioclase >50%, quartz, and amphibole <10%) and textures (quartz-plagioclase graphic and vermicular intergrowth textures) of the El-Shadli granite are typical of plagiogranites³ (Fig. 3e, f-I and Supplementary Figs 2 and 3). In addition, the compositions plot in the trondhjemite and tonalite low-pressure fields on the Ab-An-Or diagram^{41,42} (Fig. 4a). The rock association of the El-Shadli complex (trondhjemite, tonalite, diorite, and gabbro) is typical of plagiogranites found in MOR and ophiolites^{3,5-8,10} (Fig. 4a and Supplementary Fig. 12a).

Geochemically, the El-Shadli granitoids have very low K_2O contents (<1 wt. %), typical of known plagiogranite rock suites worldwide (Fig. 4b), suggesting a low-K mafic source⁴³ (Fig. 4c). On discrimination diagrams of Rb vs. Y + Nb and Nb vs. Y⁴⁰, the El-Shadli granites plot in the ORG (ocean ridge granite) field, which is typical of plagiogranites from ocean ridge settings (Fig. 4d and Supplementary Fig. 12b). In addition to their high contents of Y (38–98 ppm), and low Nb (0.78–2.83 ppm), they are low in Rb (a fluid-mobile element) (2.06–13.45 ppm; average = 6.5 ppm) (Fig. 4d and Supplementary Fig. 12b) indicating derivation from a highly depleted source and no interaction with (or contamination by) continental crustal materials. Such geochemical features are typical of the MOR- and/or oceanic plume-related granites⁴⁰ (Fig. 4d, Supplementary Fig. 12b, and Supplementary Data 1).

Other geochemical features typical of plagiogranites are the flat REE patterns^{2,3,5,7,8,10} (Fig. 5a, b), low Sr (43–200 ppm), low Rb/Sr (0.02–0.21), and low Sr/Y ratios (0.44–5.29)^{2,3,5}. Their low abundance of LILE such as Cs, Rb, Ba, Th, and U also distinguishes them from arc-related granitoids and demonstrates

a lack of interaction between the parental magma and subducting crustal and sedimentary materials⁴⁰ (Supplementary Fig. 6). These geochemical features therefore suggest that the El-Shadli granitoids have a different origin and formed in a different geodynamic setting from other coeval ANS granitoids^{44,45} (Figs 4 and 5 and Supplementary Figs 5, 6, and 12).

Zircon trace-element contents are a powerful tool for tracking the origin of granites and for distinguishing between the different granitic types³⁸. Chondrite-normalized REE patterns of the El-Shadli zircon grains plot in the ocean-crust zircon field, as defined by zircons from oceanic crust plagiogranites and gabbroic rocks³⁸ (Supplementary Fig. 9). Also, the low U/Yb and Gd/Yb of the El-Shadli zircon grains are similar to MOR plagiogranite zircons³⁸ (Fig. 7a, b and Supplementary Fig. 10a). Their $\delta^{18}\text{O}$ values of 4.52 ± 0.14 to $4.83 \pm 0.09\text{‰}$ extend ~1‰ below values typical of mantle zircon ($5.3 \pm 0.3\text{‰}$)⁴⁶ and are similar to $\delta^{18}\text{O}$ values of plagiogranites (Fig. 7d and Supplementary Fig. 10c), which range from 3.9 to 5.6‰ (average = $4.9 \pm 0.6\text{‰}$)⁷.

In conclusion, the mineralogical, petrological, and geochemical characteristics of the El-Shadli granites indicate that they are plagiogranites, which clearly distinguishes them from known ANS I- and A-type granites^{44,45}, trondhjemite-tonalite-granodiorite suites⁴⁷, and arc-related granitoids⁴⁰ (Figs 4, 5, and 7 and Supplementary Figs 5, 6, 10, and 12).

Characteristics of the melt source. The El-Shadli plagiogranites have MORB-like compositions. They are metaluminous, have very low K_2O (Fig. 4b and Supplementary Data 1), and flat-like CI-normalized (except for sample R11-1) REE patterns with slight LREE depletion relative to HREE [$(\text{La}/\text{Yb})_N = 0.41\text{--}0.88$] (Fig. 5a). The low initial $^{87}\text{Sr}/^{86}\text{Sr}$ ratios and high positive $\epsilon\text{Nd}(t)$ of the El-Shadli plagiogranites and associated gabbros

(Supplementary Fig. 7) indicate the juvenile composition of a source rock that was itself extracted from a depleted MORB-like mantle source.

The Sr-Nd isotopic data of the El-Shadli plagiogranites and associated gabbros, as with the overlying El-Shadli bimodal volcanics²³, are comparable to the nearby ~750 Ma W. Gerf and W. Ghadir N-MORB mafic ophiolites^{24,48} (Supplementary Fig. 7). Collectively, the geochemical and isotopic characteristics of the El-Shadli plagiogranites and associated gabbros suggest derivation from a MORB-like depleted source, similar to that of the El-Shadli bimodal volcanics²³. These characteristics are all typical of plagiogranites that are generally interpreted to reflect juvenile and depleted sources^{2,3,5,7,8,10,40}. The enrichment in some LILE (Cs, Rb, Ba, Th, and U) in the El-Shadli plagiogranites and associated gabbros relative to N-MORB are likely an inherited feature and could be related to hydrothermal alteration of their source in the oceanic crust^{11,49}. The same enrichments in these LILE have been reported in the nearby ~750 Ma W. Gerf and W. Ghadir N-MORB mafic ophiolites^{24,48}.

The juvenile El-Shadli plagiogranite lithochemistry, together with the absence of pre-Neoproterozoic zircon inherited cores or xenocrysts in any of the samples (Fig. 6 and Supplementary Fig. 9), implies that there is no evidence for interaction with old crustal materials⁷. The low U/Yb ratios (mostly <0.1) of the El-Shadli plagiogranite zircons are similar to modern ocean-crust zircons from a depleted source with MORB-like composition and contrasts with continental and arc zircons³⁸ (Fig. 7a, b and Supplementary Fig. 10a). The low Nb/Yb and Gd/Yb ratios of the El-Shadli plagiogranite zircons are also well-defined features of zircon extracted from a

depleted MORB-like source^{23,38} (Fig. 7b and Supplementary Fig. 10a). The high positive ϵHf_t values (weighted mean from $+10.82 \pm 0.17$ to $+11.56 \pm 0.51$) of the El-Shadli plagiogranite zircons (Fig. 7c and Supplementary Fig. 10b) also indicate a juvenile source with no measurable contribution from old continental crust^{50,51}. These data indicate the El-Shadli plagiogranites were derived from a highly depleted source and indicate a different mode of origin from that of the coeval ANS granitoids⁴⁴ (Fig. 7c). It is worth noting that the felsic endmember (sample S02-5) of the overlying ~700 Ma El-Shadli bimodal volcanics shares the same zircon isotopic and trace-element characteristics as the plagiogranite, suggesting derivation from a similarly depleted MORB-like source²³ (Fig. 7).

The uniform $\delta^{18}\text{O}$ values (weighted mean from 4.52 ± 0.14 to $4.83 \pm 0.09\text{‰}$) of the El-Shadli plagiogranite zircons are lower than that of typical mantle values ($5.3 \pm 0.3\text{‰}$)⁴⁶ but are consistent either with a source that has previously undergone interaction with high-temperature hydrothermal fluids or with sub-solidus alteration of plagiogranite by post-magmatic fluid-rock interaction^{7,9} (Fig. 7d and Supplementary Fig. 10c). The former possibility is favored for several reasons. First, petrographic observations and the low LOI indicate the plagiogranites are very fresh. Second, zircon resists post-magmatic modification, and zircon within the plagiogranite preserves primary magmatic signatures such as crystal shapes with oscillatory zoning (Fig. 6 and Supplementary Fig. 8), high Th/U (mostly >0.4)⁵², and U contents mostly <1000 ppm^{37,52} (Supplementary Fig. 11 and Supplementary Data 1). In addition, there is no correlation between Th/U and U vs. $\delta^{18}\text{O}$ (Supplementary Fig. 11), and our U-Pb data yield concordant to nearly concordant ages (Fig. 6 and

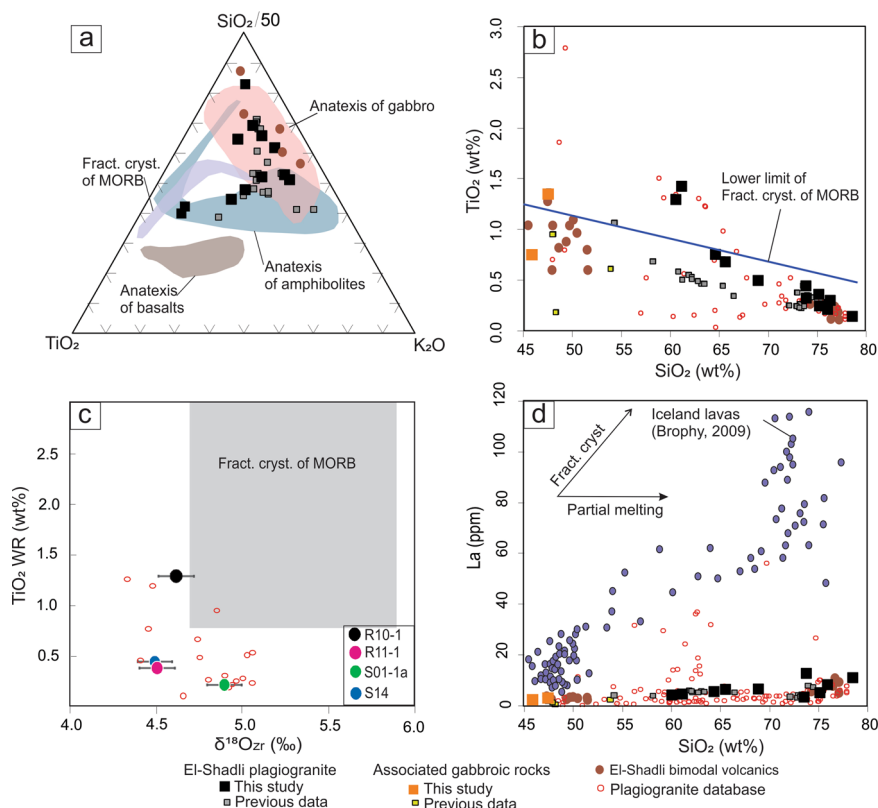


Fig. 8 Whole-rock petrogenetic discrimination diagrams. **a** Ternary diagram of $\text{TiO}_2\text{-SiO}_2/50\text{-K}_2\text{O}$ modified after France et al.¹⁷ based on experimental work to evaluate the composition of plagiogranitic melts resulting from fractional crystallization of MORB⁵⁵ and partial melting of hydrated oceanic crust (i.e., gabbros, amphibolites, and basalts)^{15,17,54}. **b** TiO_2 (wt%) vs. SiO_2 (wt%) diagram¹¹ showing the lower limit for plagiogranitic melts resulting from fractional crystallization of MORB. **c** TiO_2 WR (wt%) vs. $\delta^{18}\text{O}_{\text{Zr}}$ (‰) diagram⁷ showing the field of plagiogranites produced by fractional crystallization of MORB. Error bars represent 2 sigma. **d** La (ppm) vs. SiO_2 (wt%) diagram was modified after Brophy¹⁶, suggesting a partial melting origin for the studied rocks. Global plagiogranite database is as referenced in the text and data for the El-Shadli bimodal volcanics are that of Gamal El Dien et al.²³.

Supplementary Fig. 9). All these features indicate that the $\delta^{18}\text{O}$ compositions may be attributed to hydrothermal fluid contamination of their source rock^{7,9}, rather than to post-magmatic alteration processes.

In summary, the whole-rock petrological, geochemical, and isotopic data and zircon U-Pb-Hf-O-trace-element data suggest that the El-Shadli plagiogranites were derived from a MORB-like, highly depleted mafic source that had previously undergone hydrothermal alteration in an oceanic-and/or ridge/rift-related setting.

Petrogenesis of the El-Shadli plagiogranites. The genesis of the plagiogranites is commonly attributed to either (a) a direct mantle-derived basaltic melt that fractionated to yield plagiogranite compositions^{2,4,53} or (b) the product of partial melting of a hydrothermally altered depleted mafic lower oceanic crust^{7,11,13,15–17,54}, both in MOR environments.

Experiments show that the composition of plagiogranitic melt resulting from fractional crystallization of MORB⁵⁵ differs markedly from that of plagiogranite melt generated by partial melting of gabbros and amphibolites from the lower oceanic crust and oceanic crustal basalts^{15,17,54,56}, particularly with regard to TiO_2 , SiO_2 , and K_2O contents (Fig. 8a). The El-Shadli plagiogranites have a compositional range that overlaps with melts produced by partial melting of hydrated gabbroic and amphibolitic rocks of the lower oceanic crust (Fig. 8a). The TiO_2 content of plagiogranitic melts derived by fractionation from tholeiitic magmas is controlled by source composition and redox conditions^{11,55}. Experiments on tholeiitic primitive MORB melts⁵⁵ show that Fe-Ti oxides are generally stable under oxidizing conditions, and so SiO_2 -enriched felsic melts have significantly lower Ti contents. On the other hand, under reducing conditions, the felsic melts produced by fractionation are characterized by high TiO_2 and FeO contents. As the differentiation of MORB melts typically occurs under more reducing conditions, the resultant felsic melts should have high Ti contents^{11,55}. In contrast, gabbros in the lower oceanic crust are highly depleted in Ti, and partial melting of this source generally occurs under hydrous (i.e., oxidizing) conditions¹⁵. The resulting felsic melts should, therefore, have very low Ti contents¹⁵. Thus, Koepke et al.^{11,15} proposed that the TiO_2 content of plagiogranites is a powerful indicator for discriminating between the more felsic plagiogranitic melts generated from anatexis of oceanic lower crustal gabbroic rocks ($\text{TiO}_2 < 1$ wt. %) and those generated by fractionation of MORB melts ($\text{TiO}_2 > 1$ wt. %). The El-Shadli trondhjemitic and tonalitic rocks have TiO_2 concentrations below the lower limit for experimental melts produced during MORB fractionation, again supporting an origin involving partial melting of mafic (gabbroic) crust (Fig. 8b, c).

Based on theoretical modeling, Brophy¹⁶ proposed that plagiogranitic melts formed by hydrous partial melting and exhibit either a flat or slightly decreasing REE with increasing SiO_2 content. Their REE patterns can be slightly higher, and/or overlap with, co-magmatic mafic rocks. On the other hand, plagiogranitic melts produced by fractional crystallization show a positive correlation between REE and SiO_2 contents¹⁶. The El-Shadli plagiogranites and associated gabbroic rocks have similar and overlapping flat REE patterns (Fig. 5a) and lack a positive correlation between La and SiO_2 (Fig. 8d), features typical of melts formed by hydrous partial melting of lower oceanic crust¹⁶. This process contrasts with that of the Iceland lavas, which display a positive correlation between La with SiO_2 from mafic to felsic endmembers and are thought to have been formed by fractional crystallization¹⁶.

Koepke et al.^{11,15} proposed that hydrous partial melting of pre-existing gabbros produces a plagiogranitic melt with amphibole as residual phase (Olivine + clinopyroxene + plagioclase (A) +

$\text{H}_2\text{O} = \text{amphibole} + \text{orthopyroxene} + \text{plagioclase (B)} + \text{plagiogranitic melt}$). As REE abundances (particular LREE to MREE) and HFS elements such as Nb are very sensitive to the presence of amphiboles in the residue, the resultant melt should be depleted in LREE and Nb^{6,11,15,54}. This is indeed the case for the El-Shadli plagiogranites (Fig. 8d and Supplementary Fig. 6). The lack of HREE depletion (Fig. 5a) indicates the absence of residual garnet, implying partial melting occurred in a low-pressure environment (i.e., in plagioclase stability field).

Zircon $\delta^{18}\text{O}$ values can also distinguish between plagiogranitic rocks generated by fractional crystallization (typical mantle-like $\delta^{18}\text{O}$ values of $5.2 \pm 0.5\text{‰}$)⁷ and those generated by re-melting of hydrothermally altered gabbroic lower oceanic crust ($\delta^{18}\text{O} = 4.9 \pm 0.6\text{‰}$)⁷. The El-Shadli zircons have low $\delta^{18}\text{O}$ values ranging between 4.52 and 4.83‰ (Fig. 7d and Supplementary Fig. 10c). There are two possible ways to cause such low $\delta^{18}\text{O}$ values: one is by melting hydrothermally altered source rocks, and the other is by assimilating hydrothermally altered wall rock during magma intrusion^{7,9}. However, a plagiogranitic magma contaminated by wall-rock assimilation would be expected to contain zircon xenocrysts and Hf-O isotopic data comparable to that upper crustal rocks⁹, but neither of these features have been observed in the studied rocks (Fig. 7d). Also, normal oceanic crust is characterized by $\delta^{18}\text{O}$ values as low as 2‰ for the gabbroic lower crust due to interaction of the mafic magma with hydrothermal fluids^{7,14}. The systematic low $\delta^{18}\text{O}$ values are typical of global ophiolitic plagiogranites, indicating that these values are primary signatures and reflect partial melting of the lower oceanic crust without overprinting by late, low-temperature fluids⁷. The above observations support the formation of the El-Shadli plagiogranites by re-melting of altered gabbroic lower oceanic crust. On the plot of TiO_2 (WR) vs. $\delta^{18}\text{O}_{\text{Zr}}$ (Fig. 8c), the El-Shadli plagiogranites also plot outside the field characterizing plagiogranites with a fractional crystallization origin but overlap with plagiogranites with a known partial melting origin from the Oman and Troodos ophiolites^{7,57}.

It has been demonstrated that high-temperature hydrothermal fluids can penetrate to upper mantle depths, and are thus capable of interacting with the oceanic gabbroic lower crust⁴⁹. The circulation of such hydrothermal fluids has been recognized by their seawater signatures such as high radiogenic $^{87}\text{Sr}/^{86}\text{Sr}$ values and high Cl and B contents in basaltic glass from MORB and secondary amphibole in the gabbroic section of ophiolites^{11,15,17,49,54}. The penetration of such hydrothermal fluids is facilitated by high-temperature shear zones/detachment fault systems in the oceanic crust^{15,49}.

Field observation of irregularly shaped enclaves of gabbroic blocks within the plagiogranite indicate the presence of magmatic mingling (Fig. 3a, a-I and Supplementary Fig. 1b). Such contact relationships are typical of mingling between two contemporaneous magmas⁶. Their interpreted coeval origin is further supported by the overlapping ages for the two rock types (Fig. 6 and Supplementary Fig. 9). The El-Shadli gabbroic rocks exhibit an evolved signature, characterized by low Mg# [$\text{MgO}/(\text{MgO} + \text{FeO}^{\text{T}}) \times 100 < 60$], Cr (<500 ppm), and Ni (<100 ppm) (Supplementary Data 1). Such low values are significantly lower than that of primary mantle melts (Ni > 500 ppm, Cr > 1000 ppm, and Mg# > 72)⁵⁸ and suggest these gabbroic rocks are not primary mantle melts. These characteristics, together with the negative correlation of SiO_2 with MgO and CaO (Supplementary Fig. 4), indicate that the source rock of the mafic magmas underwent olivine and clinopyroxene fractionation. Thus, the magma compositions of the gabbroic rocks originated by extensive partial melting of a depleted, juvenile mafic source.

Collectively, whole-rock petrology, geochemical and isotopic data, and zircon Hf-O isotopes support partial melting of the hydrated gabbroic lower oceanic crust as the origin for the El-

Shadli plagiogranites. Some “arc-like” trace-element patterns, such as Nb and Ti negative anomalies, and LILE enrichment, can be interpreted as the result of (1) hydrothermal fluid contamination of the source rocks and/or (2) a two-stage process (i.e., generation followed by re-melting of highly depleted source) for the production of the plagiogranitic melt.

Geodynamic context and formation mechanism for the El-Shadli plutonic complex. The geochemical and isotopic data distinguish the El-Shadli plagiogranites from other arc-related granitoids (Figs 4, 5, and 7 and Supplementary Figs 6, 10, and 12) and suggest their formation in a ridge/within-plate tectonic environment (Fig. 4d and Supplementary Fig. 12b). The El-Shadli plutonic complex (plagiogranites and associated gabbros) intruded pre-existing poly-deformed and variably metamorphosed ophiolitic complexes, as evidenced by cross-cutting relationships with strongly foliated ophiolitic country rocks (Fig. 2). The lack of significant deformation or metamorphism in the El-Shadli plutonic complex is consistent with its emplacement in a within-plate tectonic setting. In addition, the El-Shadli plutonic complex is overlain by rift-related, within-plate, and slightly younger (~700 Ma) bimodal volcanic rocks^{23,27} (Fig. 2). These relationships further support a post-accretionary, within-plate/rifting tectonic setting for the El-Shadli plutonic complex. Geochemical and isotopic data for the El-Shadli plagiogranites suggest an origin involving the anatexis of hydrated gabbroic lower oceanic crust. Their highly depleted and juvenile composition indicates that the magma was likely derived from partial melting of a juvenile mafic proto-continental crust (i.e., accreted oceanic crust) along a continental margin (Fig. 9b, c). This juvenile mafic proto-continental crust was accreted along the flanks of an ocean (i.e., the Mozambique Ocean) that bordered the Rodinia supercontinent (Fig. 9b, c). Such accreted mafic juvenile crust was likely thinner and denser than normal continental crust and was thus mostly submerged (Fig. 9b, c), thereby explaining the submarine setting of the slightly younger (~700 Ma) bimodal volcanics and the formation of pillow basalts^{23,27}. The El-Shadli plagiogranites were formed by melting of an oceanic crust that was accreted 20–10 Myr earlier (i.e., by melting of older ophiolitic complexes), unlike other plagiogranites found in ophiolites and MOR settings worldwide, in which plagiogranites formed contemporaneously with MOR magmatism^{2,4,57}.

It has been suggested that the volume of plagiogranites reflects the formation process (fractional crystallization vs. partial melting)¹⁵. Fractional crystallization of basaltic magma normally produces small volumes of plagiogranites in MOR environments^{4,7,15}. On the other hand, larger volumes of plagiogranitic melt can be generated by partial melting processes and are more likely to occur in ophiolites^{7,15}. Such partial melting processes are made possible by high H₂O activity and possibly with an excess heat source in MOR environments. The H₂O could be provided through penetration of hydrothermal fluids from the ocean via high-temperature detachment fault systems/shear zones along the MOR^{15,49} (Fig. 9a). The excess heat source is generally believed to have been provided by underlying melt lenses beneath the MOR^{6,15,54}, but Amri et al.⁵ suggested an upwelling mantle diapir as a heat source for the formation of the largest plagiogranites (up to 8 km in outcrop dimension) within the Oman ophiolites. As the El-Shadli plagiogranites formed after terrane accretion instead of in a MOR environment, and the 730–700 Ma magmatism is coeval with global continental rifting and the break-up of Rodinia (~825–680 Ma)^{59,60}, the heat source for their formation could have been related to emplacement of a mantle plume during Rodinia break-up^{59,60} (Fig. 9c), as first speculated by Gamal El Dien et al.²³ for the formation of the ~700 Ma rift volcanics found in the same region. Given that the El-Shadli plagiogranites formed in a post-accretionary within-plate setting,

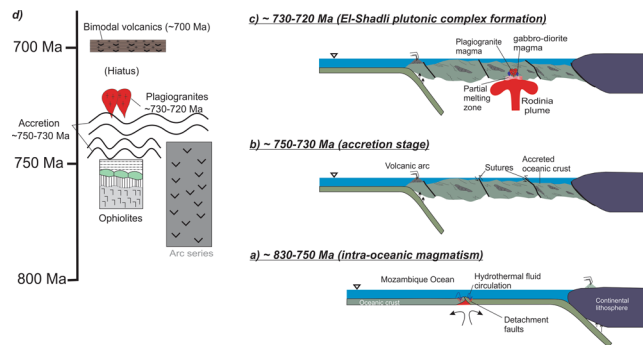


Fig. 9 A tectonic model for the formation of the El-Shadli plutonic complex (modified after Gamal El Dien et al.²³). **a** Oceanic spreading and subduction along a continental arc during ~830–750 Ma, highlighting hydrothermal fluids circulating and altering the lower oceanic crust near MOR. **b** Accretion of oceanic terranes (including oceanic arcs) during ~750–730 Ma, forming a juvenile proto-continental crust. **c** Formation of the El-Shadli plagiogranites and associated gabbros above asthenosphere upwelling possibly driven by a mantle plume at ~730–720 Ma by partial melting the accreted lower oceanic crust. **d** Tectonostratigraphic column of the study region.

the mantle upwelling could also have been induced by slab break-off⁶¹. However, the composition of the El-Shadli plutonic complex is inconsistent with granitoid magmas produced by slab break-off⁶² (Fig. 4d). Thus, a plume-induced model²³ is preferred based on evidence discussed below.

First, the exceptional large volume of the El-Shadli plagiogranite (a lateral dimension of ca. ~100 km × 50 km) can best be explained by mantle plume-induced large-scale re-melting the accreted mafic lower crust that generated both the super-large El-Shadli plagiogranites and the overlying bimodal volcanics (80 km × 35 km with a thickness of >10 km)^{23,27}. Second, there is evidence for mantle plume activity of that age in the region, such as the layered mafic-ultramafic intrusions at Korab Kansi (741 ± 24 Ma)⁶³ and at G. Dahanib (710 ± 7 Ma)⁶⁴ (Fig. 1b). Third, the hiatus between the 730–720 Ma plagiogranite and the overlying ~700 Ma bimodal rift volcanics (Fig. 9d) can be interpreted as plume-induced regional doming^{23,65}.

As plumes tend to preferentially nucleate along the margins of a superplume⁶⁶, a plume heat source is in accord with the proposed paleogeographic position of the ANS over the edge of the Rodinia superplume during the break-up/continental rifting of the supercontinent Rodinia between 825 and 680 Ma^{59,60}. Coeval plume-related magmatism along the margins of Rodinia including granitoids, mafic-ultramafic dikes, and rift-related bimodal volcanics found in South China, Australia, Southern Africa, and Laurentia^{60,67,68}. The proposed plume-induced model for the El-Shadli plutonic complex (~730–720 Ma) is coeval with the global plume/rift-related magmatism such as the well-known Franklin large igneous provinces event (~727–720 Ma) in Laurentia^{60,68} that extend until ~712 Ma⁶⁹, and the Gannakouriep event (~720 Ma) in South Africa and Namibia⁶⁷.

In summary, we propose that the exceptionally large El-Shadli plagiogranite was formed by partial melting of previously accreted oceanic crust (juvenile proto-continental crust) above a mantle plume, instead of the previously well-known formation mechanisms in MOR environments. The preferred tectonic model (Fig. 9) also has implications for the crustal growth of the ANS. Most previous models focus on arc accretion^{18,20}, but mantle plume and rift-related-magmatism have also been suggested to have played an important role in crustal evolution^{21,22}. However, previous studies^{21,22} advocating plume involvement only inferred that it occurred within an oceanic environment (i.e., the formation of

oceanic plateaus) before accretion and that the products of plume activity were subsequently accreted with island arcs to form a juvenile continental crust. The model presented herein, modified from Gamal El Dien et al.²³, suggests that plumes may have also been important in the post-accretionary evolution of the ANS. Our model emphasizes the importance of mantle plume emplacement in the transformation of newly accreted ANS Neoproterozoic juvenile crust into a coherent normal continental crust by promoting intensive crustal re-melting, and possibly by the addition of new melts from the mantle into the crust. As the ANS represents one of the largest post-Archaeon juvenile continental crustal growth events on Earth, our new mechanism for the formation of plagiogranite and the transformation of accreted juvenile terranes into consolidated and stratified normal continental crust could potentially serve as an analog to the early crust formation on early Earth.

Methods

Sampling and petrological examination. Rock samples were mostly collected along W. Ranga (samples R10-1, 2 and R11-1, 2), W. Huluz (samples S01-1a, b), W. Durunkat (samples S23-1, 2, S24, and S25-1, 2), and W. Abu Hammamid (sample S14) (Fig. 2). Samples from previous work on the batholiths^{30,70} covered the areas of W. El Ridi, W. Ranga, W. Abu Ghalaga, W. Dabbah, and W. Abu Ghusun (Fig. 2). Sample locations and coordinates are provided in the geological map (Figs 1 and 2) and Supplementary Data 1, respectively. The geological map is created using ArcGIS Desktop 10.7 licensed to Curtin University.

Thin sections of the rock samples were cut and polished with progressively finer grades of diamond paste (9–1 µm thick) by service provider Yu'neng Petrology and Mineral Service Company, China. The relative abundance of minerals (both transparent and opaque) and their textural relationships were determined on a Nikon Eclipse optical microscope at Curtin University using transmitted and reflected light. Also, whole thin section images were collected for some samples using a Zeiss Axio Imager M2m Imaging System at Curtin University, at 5× magnification under transmitted and reflected light.

Phase mineral distribution maps for samples R10-1, R11-1, S01-1a, S14, S23-1, S23-2, S24, S25-1, and S25-2 were acquired using a TESCAN Integrated Mineral Analyzer (TIMA) housed at the John de Laeter Centre, Curtin University (Supplementary Fig. 2). The analysis was performed on carbon-coated whole thin sections using Liberation analysis in “Dot Mapping” mode adopting 3 µm dot spacing for backscattered electron images and 27 µm for X-ray acquisition operating at 25 kV acceleration voltage, 15 mm working distance, and a magnification of 185 times. Data processing (include calculation of modal composition) was performed with the TESCAN TIMA version 1.6.71 software.

Whole-rock major and trace-element geochemistry. Rock samples were examined first by optical microscopy. Selected rock samples were crushed with a polyethylene-wrapped hammer into <0.5 cm small chips, ultrasonically cleaned in distilled water, and subsequently dried and handpicked to avoid altered pieces and visible contamination. The samples were then ground with ethyl alcohol in an agate ring mill to grain size <50 µm, and the resulting powders were used for the analyses of major and trace elements, and Sr–Nd isotopes (Supplementary Data 1).

Whole-rock major element oxides were determined by XRF at Bureau Veritas Lab, Perth, Western Australia. Each whole-rock sample was pulverized in a vibrating disc pulverizer. The sample powder was ignited at 1000 °C for 2 h to determine the LOI using a robotic TGA system. Subsequently, the sample was cast using a 66:34 flux with 4% lithium nitrate to form a glass pill (fuse bead) by melting at 1080 °C. The major oxides (Al₂O₃, Cr₂O₃, Fe₂O₃, K₂O, MgO, MnO, Na₂O, P₂O₅, SiO₂, and TiO₂) were determined using XRF on the oven-dried (105 °C) fuse beads.

The trace and REE of the samples were analyzed using an Agilent 7500 quadrupole ICPMS at Macquarie (MQ) GeoAnalytical lab, Macquarie University, Australia. Acid digestion with hydrofluoric acid (HF) was used to digest geological materials for trace-element determination. Powdered samples of 100 mg each were weighed into 15 mL Saville Teflon beakers. The samples were first refluxed in 1.5 mL conc. HF (Merck Suprapur grade) + 1.5 mL of Teflon distilled HNO₃ at 130 °C overnight, then ultrasonicated and dried. This process was repeated and then ten drops of conc. HClO₄ (Merck Suprapur) and 2 mL of conc. HF (Merck Suprapur) was added and evaporated to incipient dryness at 170 °C before adding five drops of conc. HClO₄. The sample beakers were tightly capped and placed on a hot plate for 24 h at 190 °C, then cooled to room temperature. Samples were finally refluxed in 2 mL of 6 N distilled HCl at 150 °C for 3 h and dried down at 190 °C, and then reflux again in 2 mL of 6 N distilled HNO₃ at 150 °C for 3 h. For trace-element analyses, the samples were diluted in 100 mL of 2% HNO₃ + 0.5% HF, and heated at 80 °C until a clear solution resulted. Reference materials BCR-2 (basalt), BHVO-2 (basalt), BIR-1 (basalt), and GSP-2 (granodiorite) were analyzed at the beginning and end of each analytical session, and their measured values agree with recommended GeoRem (<http://georem.mpch-mainz.gwdg.de>) and USGS values.

The precision of the measurements by repeated analyses of reference samples is better than ±5% for trace elements and REEs.

Whole-rock Sr–Nd isotopes. Sr and Nd isotopic ratios were obtained by thermal ionization mass spectrometry (TIMS) on a Thermo Finnigan Triton system at Macquarie (MQ) GeoAnalytical Lab, Macquarie University. Analytical procedures including cleaning and column preparation, sample digestion, chromatographic separation to collect Sr and Nd, and sample loading on Re filament and data collection from TIMS are detailed in Tilhac et al.⁷¹. BHVO-2 reference material was first measured in each analytical session to check instrument status and sensitivity for Sr and Nd and was followed by unknown samples. Ratios were normalized to ⁸⁶Sr/⁸⁸Sr = 0.1194 and ¹⁴⁶Nd/¹⁴⁴Nd = 0.7219 to correct for mass fractionation. BHVO-2 yielded ⁸⁷Sr/⁸⁶Sr ratios ranging between 0.703449 ± 0.000290 (2σ) and 0.703486 ± 0.000464 (2σ) and ¹⁴³Nd/¹⁴⁴Nd between 0.512952 ± 0.000346 (2σ) and 0.512993 ± 0.000106 (2σ). These values are within the range of GeoRem preferred values for BHVO-2 (⁸⁷Sr/⁸⁶Sr = 0.703469 ± 0.000034; ¹⁴³Nd/¹⁴⁴Nd = 0.512979 ± 0.000014). Blanks were below 1000 pg for Sr and 80 pg Nd. ⁸⁷Rb/⁸⁶Sr and ¹⁴⁷Sm/¹⁴⁴Nd were calculated using the elemental ratios measured by solution ICPMS for the whole rock. The initial ⁸⁷Sr/⁸⁶Sr and ¹⁴³Nd/¹⁴⁴Nd ratios were calculated using λ⁸⁷Rb = 1.42 × 10⁻¹¹ and λ¹⁴⁷Sm = 6.55 × 10⁻¹² and the assigned U–Pb zircon ages were collected from SHRIMP and LASS for each sample. The ¹⁴³Nd/¹⁴⁴Nd isotopic ratios are given as epsilon (ε) notations relative to chondritic uniform reservoir (CHUR) (¹⁴³Nd/¹⁴⁴Nd = 0.512630 and ¹⁴⁷Sm/¹⁴⁴Nd = 0.196³⁶).

$$\epsilon\text{Nd}_{(t)} = [({}^{143}\text{Nd}/{}^{144}\text{Nd}_{\text{sample}})/({}^{143}\text{Nd}/{}^{144}\text{Nd}_{\text{CHUR}}) - 1] \times 10,000.$$

Zircon mount preparation. Zircon grains were separated from crushed rock samples (1–5 kg/each) using standard methods (Frantz magnetic separator and heavy liquids) at Yu'neng Petrology and Mineral Service Company, China. The best-quality grains, characterized by homogenous transparency, color, and fluorescence, were handpicked and mounted in 24 mm diameter epoxy resin discs and polished to expose the interior of the grains. Zircon grains from each sample were mounted along with zircon standards for age calibration (Plešovice) and O isotopes (Penglai and Qinghu) in Guangzhou Institute of Geochemistry, Chinese Academy of Sciences (GIGCAS). The zircon crystals were characterized by CL imaging using a Tescan MIRA3 scanning electron microscope in the Microscopy and Micro-analysis Facility, John de Laeter Centre, Curtin University using 12 kV, spot size 6 µm, and working distance ~15 mm (Supplementary Fig. 8). In the CL images, high-U regions appear as dark regions, and low U regions appear as bright regions. Analytical spots, selected through CL imaging, were transparent, smooth, and without obvious inclusions. The polished mounts were cleaned in high-purity ethanol using an ultrasonic bath, and then vacuum-coated with high-purity gold before the SHRIMP and SIMS analyses.

SHRIMP U–Pb zircon analyses. Zircon U–Pb isotope measurements were done on the SHRIMP II instrument at the John de Laeter Centre, Curtin University (Supplementary Data 2). Curtin ion-microprobe SHRIMP II analytical procedures broadly followed those described by Compston et al.⁷² and Williams⁷³. A 25–30 µm diameter spot size was used for all the analyzed grains with a primary beam current of 2.5–3.0 nA, mass resolution of ~5000, and analysis sensitivity of ~18 cps ppm⁻¹ nA⁻¹. Data for each spot were collected in sets of six scans through the mass range of ¹⁹⁶ZrO⁺, ²⁰⁴Pb⁺, background, ²⁰⁶Pb⁺, ²⁰⁷Pb⁺, ²⁰⁸Pb⁺, ²³⁸U⁺, ²⁴⁸ThO⁺, and ²⁵⁴UO⁺. The measured isotopic ratios were corrected for common Pb based on the measured ²⁰⁴Pb and using the two stages common Pb evolution curve of Stacey and Kramers⁷⁴ to get the common Pb compositions. Multiple standard analyses were interspersed between analyses during each session (once every four unknowns). Pb/U ages were normalized to a recommended value of 337.1 Ma determined by conventional U–Pb analysis of Plešovice zircon standard⁷⁵. The measurement of ²⁰⁶Pb/²³⁸U and ²⁰⁷Pb/²³⁵U ages requires normalization to results of the standard analyses, and the reported results were corrected for the uncertainties associated with the measurements of the Plešovice standard. The correction formula for Pb/U fractionation is ²⁰⁶Pb/²³⁸U⁺ = a(²³⁸U/¹⁶O⁺/²³⁸U⁺)^{b76} using the parameter values of Black et al.⁷⁷ All isotopic measurements were reduced, processed, and interpreted using SQUID II, Isoplot, and Isoplot R programs^{78–80}. The errors associated with individual analyses are 1σ uncertainties and include errors from U–Pb calibration based on the reproducibility of U–Pb standard measurements, counting statistics, and the common Pb correction. The weighted mean ages are quoted at the 95% confidence interval (2 SD). The ages quoted through the text are ²⁰⁶Pb/²³⁸U ages that are more precise than ²⁰⁷Pb/²⁰⁶Pb ages for Neoproterozoic zircons due to the lower content of ²⁰⁷Pb in these zircons⁸¹.

Laser ablation split stream inductively coupled plasma mass spectrometry (LASS-ICPMS) zircon U–Pb, Lu–Hf isotopes, and trace-elements analyses.

Zircon U–Pb, Lu–Hf isotopes, and trace-element abundances were measured using LASS inductively coupled plasma mass spectrometry (LASS-ICPMS) in the Geo-History Facility at the John de Laeter Centre, Curtin University (Supplementary Data 3). The analyses were conducted on the same grain as the SHRIMP analysis, commonly over the same spots. Additional LASS-ICPMS spots were targeted based on CL images. The measured U–Pb and Lu–Hf isotopes and trace-element data were collected simultaneously using an excimer laser (Resonetics S-155-LR 193

nm) coupled to a Nu Plasma II multi-collector ICPMS (MC-ICPMS) and Agilent 7700s quadrupole mass spectrometer. The laser spot diameter was 50 μm , with 3 J cm^{-2} on-sample laser fluence, repetition rate of 10 Hz, ablation time of 40 s, and ~ 45 s of total baseline acquisition.

U-Pb and trace-element data were collected from the split stream on an Agilent 7700s quadrupole mass spectrometer. Analyses of unknowns were bracketed by blocks of primary and secondary zircon reference materials such as 91500, GJ-1, Plešovice, and R33 to monitor and correct for mass fractionation and instrument drift. Zircon standard 91500 (1062.4 \pm 0.4 Ma)⁸² was utilized as the primary zircon reference age standard in this study. Standards GJ-1 (608.5 \pm 0.15 Ma)⁸³, Plešovice (337.13 \pm 0.37 Ma)⁷⁵, and R33 (419.26 \pm 0.39 Ma)⁸⁴ were analyzed as secondary age standards and treated as unknowns to monitor data accuracy and precision, and were corrected for mass bias and fractionation based on measured isotopic ratios of the primary reference material. During the analytical session, 91500 gave a $^{206}\text{Pb}/^{238}\text{U}$ age of 1062.33 \pm 3.33 Ma (MSWD = 0.09, p = 1.00, n = 29, self-normalized); GJ-1 yielded a $^{206}\text{Pb}/^{238}\text{U}$ age of 602.29 \pm 1.16 Ma (MSWD = 0.89, p = 0.65, n = 30); Plešovice yielded a $^{206}\text{Pb}/^{238}\text{U}$ age of 337.46 \pm 1.00 Ma (MSWD = 0.44, p = 0.96, n = 15); and R33 yielded a $^{206}\text{Pb}/^{238}\text{U}$ age of 416.99 \pm 1.52 Ma (MSWD = 0.91, p = 0.61, n = 31). The accuracy of individual analyses was typically within 1% of the accepted value. Trace-element data were collected simultaneously, and raw data were reduced against GJ-1 using ^{91}Zr as the internal reference isotope standard, assuming 43.14% Zr in zircon.

Lu-Hf isotopic data were collected on a Nu Plasma II MC-ICPMS. Measurements of ^{172}Yb , ^{173}Yb , ^{175}Lu , ^{176}Hf + Yb + Lu, ^{177}Hf , ^{178}Hf , ^{179}Hf , and ^{180}Hf masses were made simultaneously on the Faraday array. The correction for the isobaric interference of Yb and Lu on ^{176}Hf was made following the method detailed in ref.⁸⁵. The assessment of the resultant corrected $^{176}\text{Hf}/^{177}\text{Hf}$ ratio (and ϵHf) is facilitated through an evaluation of the correlation between $^{176}\text{Hf}/^{177}\text{Hf}$ and $^{176}\text{Yb}/^{177}\text{Hf}$ or $^{176}\text{Lu}/^{177}\text{Hf}$, and a range of reference materials with varying $^{176}\text{Lu}/^{177}\text{Hf}$ and $^{176}\text{Yb}/^{177}\text{Hf}$ ratios was also analyzed to validate the isobaric interference corrections^{85,86}.

Standard-sample-standard bracketing was applied using Mud Tank ($^{176}\text{Hf}/^{177}\text{Hf}$ = 0.282505 \pm 0.000044)⁸⁷ as the primary reference material. 91500 ($^{176}\text{Hf}/^{177}\text{Hf}$ = 0.282306 \pm 0.000008)⁸⁷, R33 ($^{176}\text{Hf}/^{177}\text{Hf}$ = 0.282749 \pm 0.000046)⁸⁸, GJ-1 ($^{176}\text{Hf}/^{177}\text{Hf}$ = 0.282000 \pm 0.000005)⁸⁹, Plešovice ($^{176}\text{Hf}/^{177}\text{Hf}$ = 0.282482 \pm 0.000012)⁷⁵, and FC1 ($^{176}\text{Hf}/^{177}\text{Hf}$ = 0.282184 \pm 0.000018)⁸⁷ were used as secondary standards to monitor accuracy of internal Hf isotope corrections for all Lu-Hf analyses. During the analytical session, the following corrected $^{176}\text{Hf}/^{177}\text{Hf}$ weighted average ratios were obtained on the standards: Mud Tank ($^{176}\text{Hf}/^{177}\text{Hf}$ = 0.282507 \pm 0.000006, MSWD = 0.012, p = 1.00, n = 31), 91500 ($^{176}\text{Hf}/^{177}\text{Hf}$ = 0.282295 \pm 0.000011, MSWD = 0.56, p = 0.97, n = 29), R33 ($^{176}\text{Hf}/^{177}\text{Hf}$ = 0.282739 \pm 0.000009, MSWD = 0.41, p = 1.00, n = 28), GJ-1 ($^{176}\text{Hf}/^{177}\text{Hf}$ = 0.281999 \pm 0.000008, MSWD = 0.54, p = 0.98, n = 31), Plešovice ($^{176}\text{Hf}/^{177}\text{Hf}$ = 0.282489 \pm 0.000018, MSWD = 0.47, p = 0.96, n = 16), and FC1 ($^{176}\text{Hf}/^{177}\text{Hf}$ = 0.282161 \pm 0.000022, MSWD = 0.79, p = 0.69, n = 16). In addition, stable isotopic ratios ($^{178}\text{Hf}/^{177}\text{Hf}$ and $^{180}\text{Hf}/^{177}\text{Hf}$) can provide a powerful indication of instrument stability and the accuracy of mass bias corrections; the weighted average of stable $^{178}\text{Hf}/^{177}\text{Hf}$ and $^{180}\text{Hf}/^{177}\text{Hf}$ ratios for all analyses was 1.46733 and 1.88686, respectively, within the expected range of those ratios⁸⁵. Data were reduced in Iolite⁹⁰ and in-house Excel macros. The $\epsilon\text{Hf}(t)$ values were calculated for all data using the ^{176}Lu decay constant = 0.865×10^{-11} yr^{-1} set out by ref.^{36,39,91}. Chondritic values are after ref.^{36,39,91} $^{176}\text{Hf}/^{177}\text{Hf}$ CHUR = 0.282785 and $^{176}\text{Lu}/^{177}\text{Hf}$ CHUR = 0.0336, where CHUR indicates chondritic uniform reservoir. Depleted mantle values are after ref.^{36,39,91} $^{176}\text{Hf}/^{177}\text{Hf}$ = 0.28325 and $^{176}\text{Lu}/^{177}\text{Hf}$ = 0.0384. Two-stage Hf model ages ($T_{\text{DM}}^{\text{Crustal}}$) were calculated from the measured Lu-Hf isotopes and U-Pb ages of the zircons, whereas the calculated initial $^{176}\text{Hf}/^{177}\text{Hf}$ ratio of the zircons is projected back to the depleted mantle growth curve assuming $^{176}\text{Lu}/^{177}\text{Hf}$ value of 0.015 for the average continental crust³⁹ using the following equations⁹²:

$$\begin{aligned} {}^{176}\text{Hf}/{}^{177}\text{Hf}_{\text{Z(T)}} &= {}^{176}\text{Hf}/{}^{177}\text{Hf}_{\text{Z(0)}} - {}^{176}\text{Lu}/{}^{177}\text{Hf}_{\text{Z}} \times (e^{\lambda T} - 1). \\ {}^{176}\text{Hf}/{}^{177}\text{Hf}_{\text{CHUR(T)}} &= {}^{176}\text{Hf}/{}^{177}\text{Hf}_{\text{CHUR(0)}} - {}^{176}\text{Lu}/{}^{177}\text{Hf}_{\text{CHUR}} \times (e^{\lambda T} - 1). \\ {}^{176}\text{Hf}/{}^{177}\text{Hf}_{\text{DM(T)}} &= {}^{176}\text{Hf}/{}^{177}\text{Hf}_{\text{DM(0)}} - {}^{176}\text{Lu}/{}^{177}\text{Hf}_{\text{DM}} \times (e^{\lambda T} - 1). \\ \epsilon\text{Hf}(T) &= [{}^{176}\text{Hf}/{}^{177}\text{Hf}_{\text{Z(T)}} / {}^{176}\text{Hf}/{}^{177}\text{Hf}_{\text{CHUR(T)}} - 1] \times 10,000. \\ T_{\text{DM}} &= (1/\lambda) \times \ln [1 + ({}^{176}\text{Hf}/{}^{177}\text{Hf}_{\text{DM}} - {}^{176}\text{Hf}/{}^{177}\text{Hf}_{\text{Z}}) / ({}^{176}\text{Lu}/{}^{177}\text{Hf}_{\text{DM}} - {}^{176}\text{Lu}/{}^{177}\text{Hf}_{\text{Z}})] \\ T_{\text{DM}}^{\text{C}} &= T_{\text{DM}} - (T_{\text{DM}} - T) \times [(f_{\text{C}} - f_{\text{Z}}) / (f_{\text{C}} - f_{\text{DM}})]. \\ f_{\text{Lu/Hf}} &= {}^{176}\text{Hf}/{}^{177}\text{Hf} / {}^{176}\text{Lu}/{}^{177}\text{Hf}_{\text{CHUR}} - 1. \end{aligned}$$

where, f_{C} , f_{Z} , and f_{DM} are the $f_{\text{Lu/Hf}}$ values of the continental crust, zircon sample, and the depleted mantle, respectively. Z = analyzed zircon, CHUR = chondritic uniform reservoir; DM = depleted mantle, T_{DM}^{C} = Two-stage Hf model ages.

SIMS zircon O-isotope analyses. Zircon O isotopic compositions were measured using a Cameca IMS 1280-HR at the high-precision SIMS Laboratory of the GIGCAS, following the analytical procedures of Yang et al.⁹³ (Supplementary Data 3). The Cs^+ primary ion beam was used to sputter oxygen ions from unknown zircon samples that accelerated at 10 kV and ~ 2 nA in intensity, with the

mass resolution being ~ 2500 . The target area was ~ 20 μm in diameter that includes a 10 μm spot diameter and a 10 μm raster diameter. ^{16}O and ^{18}O isotopes were measured in multi-collector mode using two off-axis Faraday cups.

Qinghu and Penglai reference zircons^{94,95} have been used to evaluate the precision (reproducibility) and accuracy. Penglai zircons were used as external reference material to calibrate the instrumental mass fractionation (IMF). Qinghu zircons were treated as an unknown sample, which yielded a precision of 5.45 \pm 0.03‰ (2 SD; MSWD = 0.58) that is consistent with the recommended value of 5.4 \pm 0.2‰ (2 SD)⁹⁴. During each session, one Penglai zircon analysis was conducted with every five unknown spots (including a Qinghu zircon standard that was treated as an unknown). The measured $^{18}\text{O}/^{16}\text{O}$ ratios were normalized to the Vienna Standard Mean Ocean Water (VSMOW $^{18}\text{O}/^{16}\text{O}$ = 0.0020052)⁹⁶ and expressed on the $\delta^{18}\text{O}$ -scale. A recommended value of $\delta^{18}\text{O}$ = 5.31 \pm 0.10‰ (2 SD) for the Penglai zircon standard was used in this study⁹⁵, and then corrected for the IMF as follows:

$$\begin{aligned} \delta^{18}\text{O}_M &= \left(\frac{({}^{18}\text{O}/{}^{16}\text{O})_M}{0.0020052} - 1 \right) \times 1000(\text{‰}), \\ \text{IMF} &= \delta^{18}\text{O}_M(\text{standard}) - \delta^{18}\text{O}_R(\text{standard}) \\ \delta^{18}\text{O sample} &= \delta^{18}\text{O}_M - \text{IMF} \end{aligned}$$

whereas $(^{18}\text{O}/^{16}\text{O})_M$ is the raw value measured by SIMS, $(\delta^{18}\text{O})_M$ the normalized ($^{18}\text{O}/^{16}\text{O})_M$ by the value of VSMOW ($^{18}\text{O}/^{16}\text{O}$ = 0.0020052), $(\delta^{18}\text{O})_M(\text{standard})$ the measured result of standard sample, $(\delta^{18}\text{O})_R(\text{standard})$ the recommended value of the Penglai standard, and $\delta^{18}\text{O sample}$ the corrected sample value.

Data availability

All data needed to evaluate the conclusions in the paper are present in the paper and/or the Supplementary material and are publicly available at <https://doi.org/10.5281/zenodo.4732646>

Received: 29 January 2021; Accepted: 11 June 2021;

Published online: 05 July 2021

References

- Kemp, A. I. S. & Hawkesworth, C. J. Growth and differentiation of the continental crust from isotope studies of accessory minerals. In *Treatise on Geochemistry* 4 379–421 (Elsevier, 2014).
- Coleman, R. G. & Peterman, Z. E. Oceanic plagiogranite. *J. Geophys. Res.* **80**, 1099–1108 (1975).
- Coleman, R. G. & Donato, M. M. *Oceanic Plagiogranite Revisited. Developments in Petrology* (ed. Barker, F.) 6 (Elsevier Scientific Publishing Company, 1979).
- Aldiss, D. T. Plagiogranites from the ocean crust and ophiolites. *Nature* **289**, 577–578 (1981).
- Amri, I., Benoit, M. & Ceuleneer, G. Tectonic setting for the genesis of oceanic plagiogranites: evidence from a paleo-spreading structure in the Oman ophiolite. *Earth Planet. Sci. Lett.* **139**, 177–194 (1996).
- Rollinson, H. New models for the genesis of plagiogranites in the Oman ophiolite. *Lithos* **112**, 603–614 (2009).
- Grimes, C. B., Ushikubo, T., Kozdon, R. & Valley, J. W. Perspectives on the origin of plagiogranite in ophiolites from oxygen isotopes in zircon. *Lithos* **179**, 48–66 (2013).
- Haase, K. M. et al. Constraints on the magmatic evolution of the oceanic crust from plagiogranite intrusions in the Oman ophiolite. *Contrib. Mineral. Petrol.* **171** (2016).
- Wang, H. et al. Continental growth through accreted oceanic arc: Zircon Hf-O isotope evidence for granulites from the Qinling orogen. *Geochim. Cosmochim. Acta* **182**, 109–130 (2016).
- Marien, C. S., Hoffmann, J. E., Garbe-Schönberg, C. D. & Münker, C. Petrogenesis of plagiogranites from the Troodos Ophiolite Complex, Cyprus. *Contrib. Mineral. Petrol.* **174** (2019).
- Koepke, J., Berndt, J., Feig, S. T. & Holtz, F. The formation of SiO₂-rich melts within the deep oceanic crust by hydrous partial melting of gabbros. *Contrib. Mineral. Petrol.* **153**, 67–84 (2007).
- Rollinson, H. Plagiogranites from the mantle section of the Oman Ophiolite: models for early crustal evolution. *Geol. Soc. Spec. Publ.* **392**, 247–261 (2014).
- Flagler, P. A. & Spray, J. G. Generation of plagiogranite by amphibolite anatexis in oceanic shear zones. *Geology* **19**, 70–73 (1991).
- Stakes, D. S. & Taylor, H. P. Oxygen isotope and chemical studies on the origin of large plagiogranite bodies in northern Oman, and their relationship

- to the overlying massive sulphide deposits. *Geol. Soc. Spec. Publ.* **218**, 315–351 (2003).
15. Koepke, J., Feig, S. T., Snow, J. & Freise, M. Petrogenesis of oceanic plagiogranites by partial melting of gabbros: an experimental study. *Contrib. Mineral. Petrol.* **146**, 414–432 (2004).
 16. Brophy, J. G. La-sio₂ and Yb-SiO₂ systematics in mid-ocean ridge magmas: implications for the origin of oceanic plagiogranite. *Contrib. Mineral. Petrol.* **158**, 99–111 (2009).
 17. France, L., Koepke, J., Ildéfonse, B., Cichy, S. B. & Deschamps, F. Hydrous partial melting in the sheeted dike complex at fast spreading ridges: experimental and natural observations. *Contrib. Mineral. Petrol.* **160**, 683–704 (2010).
 18. Fritz, H. et al. Orogen styles in the East African Orogen: a review of the Neoproterozoic to Cambrian tectonic evolution. *J. African Earth Sci.* **86**, 65–106 (2013).
 19. Johnson, P. R. et al. Late Cryogenian-Ediacaran history of the Arabian-Nubian Shield: a review of depositional, plutonic, structural, and tectonic events in the closing stages of the northern East African Orogen. *J. African Earth Sci.* **61**, 167–232 (2011).
 20. Stern, R. J. ARC assembly and continental collision in the Neoproterozoic East African Orogen: implications for the consolidation of Gondwanaland. *Annu. Rev. Earth Planet. Sci.* **22**, 319–351 (1994).
 21. Reymer, A. & Schubert, G. Rapid growth of some major segments of continental crust. *Geology* **14**, 299 (1986).
 22. Stein, M. & Goldstein, S. L. From plume head to continental lithosphere in the Arabian-Nubian shield. *Nature* **382**, 773–778 (1996).
 23. Gamal El Dien, H. et al. Two-stage crustal growth in the Arabian-Nubian shield: initial arc accretion followed by plume-induced crustal reworking. *Precambrian Res.* **359**, 106211 (2021).
 24. Basta, F. F., Maurice, A. E., Bakht, B. R., Ali, K. A. & Manton, W. I. Neoproterozoic contaminated MORB of Wadi Ghadir ophiolite, NE Africa: geochemical and Nd and Sr isotopic constraints. *J. African Earth Sci.* **59**, 227–242 (2011).
 25. Kröner, A., Todt, W., Hussein, I. M., Mansour, M. & Rashwan, A. A. Dating of late Proterozoic ophiolites in Egypt and the Sudan using the single grain zircon evaporation technique. *Precambrian Res.* **59**, 15–32 (1992).
 26. Abdel El-Wahed, M., Kamh, S. Z., Ashmawy, M. & Shebl, A. Transpressive structures in the Ghadir Shear Belt, Eastern Desert, Egypt: evidence for partitioning of oblique convergence in the Arabian-Nubian Shield during Gondwana Agglutination. *Acta Geol. Sin. English Ed.* **93**, 1614–1646 (2019).
 27. Stern, R. J., Kröner, A. & Rashwan, A. A. A late Precambrian (710 Ma) high volcanicity rift in the southern Eastern Desert of Egypt. *Geol. Rundschau* **80**, 155–170 (1991).
 28. Kröner, A., Kruger, J. & Rashwan, A. A. Age and tectonic setting of granitoid gneisses in the Eastern Desert of Egypt and south-west Sinai. *Geol. Rundschau* **83**, 502–513 (1994).
 29. Maurice, A. E., Basta, F. F. & Khiyam, A. A. Neoproterozoic nascent island arc volcanism from the Nubian Shield of Egypt: magma genesis and generation of continental crust in intra-oceanic arcs. *Lithos* **132–133**, 1–20 (2012).
 30. Gharib, M. E. & Ahmed, A. H. Late Neoproterozoic volcanics and associated granitoids at Wadi Ranga, south Eastern Desert, Egypt: a transition from subduction related to intra-arc magmatism. *Lithos* **155**, 236–255 (2012).
 31. Gamal El Dien, H. *Geochemical Records Linking Plate Tectonics with Mantle Dynamics: Neoproterozoic and Beyond*. (Curtin University, 2020). 20.500.11937/82663.
 32. Frost, B. R. et al. A geochemical classification for granitic rocks. *J. Petrol.* **42**, 2033–2048 (2001).
 33. Anders, E. & Grevesse, N. Abundances of the elements: meteoritic and solar. *Geochim. Cosmochim. Acta* **53**, 197–214 (1989).
 34. Sun, S.-s. & McDonough, W. F. Chemical and isotopic systematics of oceanic basalts: implications for mantle composition and processes. *Geol. Soc. London, Spec. Publ.* **42**, 313–345 (1989).
 35. Goldstein, S. L., O’Nions, R. K. & Hamilton, P. J. A Sm-Nd isotopic study of atmospheric dusts and particulates from major river systems. *Earth Planet. Sci. Lett.* **70**, 221–236 (1984).
 36. Bouvier, A., Vervoort, J. D. & Patchett, P. J. The Lu-Hf and Sm-Nd isotopic composition of CHUR: Constraints from unequilibrated chondrites and implications for the bulk composition of terrestrial planets. *Earth Planet. Sci. Lett.* **273**, 48–57 (2008).
 37. Kirkland, C. L., Smithies, R. H., Taylor, R. J. M., Evans, N. & McDonald, B. Zircon Th/U ratios in magmatic environments. *Lithos* **212–215**, 397–414 (2015).
 38. Grimes, C. B., Wooden, J. L., Cheadle, M. J. & John, B. E. “Fingerprinting” tectono-magmatic provenance using trace elements in igneous zircon. *Contrib. Mineral. Petrol.* **170**, 1–26 (2015).
 39. Griffin, W. L. et al. Zircon chemistry and magma mixing, SE China: in-situ analysis of Hf isotopes, Tonglu and Pingtan igneous complexes. *Lithos* **61**, 237–269 (2002).
 40. Pearce, J. Sources and settings of granitic rocks. *Episodes* **19**, 120–125 (1996).
 41. O’Connor, J. T. A classification of quartz rich igneous rock based on feldspar ratios. *US Geol. Surv.* **525B**, B79–B84 (1965).
 42. Barker, F. T. Definition, environment and hypotheses of origin. *Dev. Petrol.* **6**, 1–12 (1979).
 43. Laurent, O., Martin, H., Moyen, J. F. & Doucelance, R. The diversity and evolution of late-Archean granitoids: evidence for the onset of “modern-style” plate tectonics between 3.0 and 2.5 Ga. *Lithos* **205**, 208–235 (2014).
 44. Robinson, F. A., Foden, J. D., Collins, A. S. & Payne, J. L. Arabian Shield magmatic cycles and their relationship with Gondwana assembly: insights from zircon U-Pb and Hf isotopes. *Earth Planet. Sci. Lett.* **408**, 207–225 (2014).
 45. Robinson, F. A., Bonin, B., Pease, V. & Anderson, J. L. A discussion on the tectonic implications of Ediacaran late- to post-orogenic A-type granite in the northeastern Arabian Shield, Saudi Arabia. *Tectonics* **36**, 582–600 (2017).
 46. Valley, J. W. et al. 4.4 billion years of crustal maturation: oxygen isotope ratios of magmatic zircon. *Contrib. Mineral. Petrol.* **150**, 561–580 (2005).
 47. Moyen, J. F. The composite Archean grey gneisses: petrological significance, and evidence for a non-unique tectonic setting for Archean crustal growth. *Lithos* **123**, 21–36 (2011).
 48. Zimmer, M., Kröner, A., Jochum, K. P., Reischmann, T. & Todt, W. The Gabal Gerf complex: a precambrian N-MORB ophiolite in the Nubian Shield, NE Africa. *Chem. Geol.* **123**, 29–51 (1995).
 49. Tao, C. et al. Deep high-temperature hydrothermal circulation in a detachment faulting system on the ultra-slow spreading ridge. *Nat. Commun.* **11**, 1–9 (2020).
 50. Belousova, E. A. et al. The growth of the continental crust: constraints from zircon Hf-isotope data. *Lithos* **119**, 457–466 (2010).
 51. Kemp, A. I. S., Hawkesworth, C. J., Paterson, B. A. & Kinny, P. D. Episodic growth of the Gondwana supercontinent from hafnium and oxygen isotopes in zircon. *Nature* **439**, 580–583 (2006).
 52. Yakymchuk, C., Kirkland, C. L. & Clark, C. Th/U ratios in metamorphic zircon. *J. Metamorph. Geol.* **36**, 715–737 (2018).
 53. Freund, S., Haase, K. M., Keith, M., Beier, C. & Garbe-Schönberg, D. Constraints on the formation of geochemically variable plagiogranite intrusions in the Troodos Ophiolite, Cyprus. *Contrib. to Mineral. Petrol.* **167**, 1–22 (2014).
 54. France, L. et al. Contamination of MORB by anatexis of magma chamber roof rocks: constraints from a geochemical study of experimental melts and associated residues. *Lithos* **202–203**, 120–137 (2014).
 55. Berndt, J., Koepke, J. & Holtz, F. An experimental investigation of the influence of water and oxygen fugacity on differentiation of MORB at 200 MPa. *J. Petrol.* **46**, 135–167 (2005).
 56. Beard, J. S. & Lofgren, G. E. Dehydration melting and water-saturated melting of basaltic and andesitic greenstones and amphibolites at 1, 3, and 6. 9 kb. *J. Petrol.* **32**, 365–401 (1991).
 57. Morag, N. et al. The origin of plagiogranites: coupled SIMS O isotope ratios, U-Pb dating and trace element composition of zircon from the Troodos Ophiolite, Cyprus. *J. Petrol.* **61** (2020).
 58. Niu, Y. & O’Hara, M. J. Global correlations of ocean ridge basalt chemistry with axial depth: a new perspective. *J. Petrol.* **49**, 633–664 (2008).
 59. Li, Z. X., Evans, D. A. D. & Halverson, G. P. Neoproterozoic glaciations in a revised global palaeogeography from the breakup of Rodinia to the assembly of Gondwanaland. *Sediment. Geol.* **294**, 219–232 (2013).
 60. Li, Z. X. et al. Assembly, configuration, and break-up history of Rodinia: a synthesis. *Precambrian Res.* **160**, 179–210 (2008).
 61. Cawood, P. A., Strachan, R. A., Pisarevsky, S. A., Gladkochub, D. P. & Murphy, J. B. Linking collisional and accretionary orogens during Rodinia assembly and breakup: Implications for models of supercontinent cycles. *Earth Planet. Sci. Lett.* **449**, 118–126 (2016).
 62. Whalen, J. B. & Hildebrand, R. S. Trace element discrimination of arc, slab failure, and A-type granitic rocks. *Lithos* **348–349**, 105179 (2019).
 63. Khedr, M. Z. et al. Petrogenesis of the ~740 Korab Kansi mafic-ultramafic intrusion, South Eastern Desert of Egypt: evidence of Ti-rich ferropicroitic magmatism. *Gondwana Res.* **82**, 48–72 (2020).
 64. Dixon, T. H. Gebel Dahanib, Egypt: a late precambrian layered sill of komatiitic composition T.H. *Contrib. Mineral. Petrol. Miner. Pet.* **76**, 42–52 (1981).
 65. Li, Z. X., Li, X. H., Kinny, P. D. & Wang, J. The breakup of Rodinia: did it start with a mantle plume beneath South China? *Earth Planet. Sci. Lett.* **173**, 171–181 (1999).
 66. Torsvik, T. H. et al. Deep mantle structure as a reference frame for movements in and on the Earth. *Proc. Natl. Acad. Sci. USA* **111**, 8735–8740 (2014).
 67. Frimmel, H. E., Hartnady, C. J. H. & Koller, F. Geochemistry and tectonic setting of magmatic units in the Pan-African Gariep Belt, Namibia. *Chem. Geol.* **130**, 101–121 (1996).
 68. Heaman, L. M., LeCheminant, A. N. & Rainbird, R. H. Nature and timing of Franklin igneous events, Canada: implications for a Late Proterozoic mantle

- plume and the break-up of Laurentia. *Earth Planet. Sci. Lett.* **109**, 117–131 (1992).
69. Denysyzyn, S. W., Halls, H. C., Davis, D. W. & Evans, D. A. D. Paleomagnetism and U-Pb geochronology of Franklin dykes in High Arctic Canada and Greenland: a revised age and paleomagnetic pole constraining block rotations in the Nares Strait region 1. *Can. J. Earth Sci.* **46**, 155–167 (2009).
 70. Maurice, A. E., Bakhit, B. R., Basta, F. F. & Khiamy, A. A. Geochemistry of gabbros and granitoids (M- and I-types) from the Nubian Shield of Egypt: roots of Neoproterozoic intra-oceanic island arc. *Precambrian Res.* **224**, 397–411 (2013).
 71. Tilhac, R. et al. Sources and timing of pyroxenite formation in the sub-arc mantle: case study of the Cabo Ortegal Complex, Spain. *Earth Planet. Sci. Lett.* **474**, 490–502 (2017).
 72. Compston, W., Williams, I. S. & Meyer, C. U-Pb geochronology of zircons from lunar breccia 73217 using a sensitive high mass-resolution ion microprobe. *J. Geophys. Res.* **89**, B525–B525 (1984).
 73. Williams, I. S. U-Th-Pb geochronology by ion microprobe. In *Applications of Microanalytical Techniques to Understanding Mineralizing Processes* (ed. McKibben, M., Shakes, W. & Ridley, W.) 7 1–35 (Society of Economic Geologists, 1998).
 74. Stacey, J. S. & Kramers, J. D. Approximation of terrestrial lead isotope evolution by a two-stage model. *Earth Planet. Sci. Lett.* **26**, 207–221 (1975).
 75. Sláma, J. et al. Plešovice zircon — a new natural reference material for U–Pb and Hf isotopic microanalysis. *Chem. Geol.* **249**, 1–35 (2008).
 76. Claué-Long, J. C., Compston, W., Roberts, J. & Fanning, C. M. Two carboniferous ages: a comparison of SHRIMP zircon dating with conventional zircon ages and $40\text{Ar}/39\text{Ar}$ analysis. In *Geochronology, Time Scales, and Global Stratigraphic Correlation* (ed. Berggren, W., Kent, D., Aubry, M.-P. & Hardenbol, J.) 3–21 (SEPM (Society for Sedimentary Geology), 1995). <https://doi.org/10.2110/pec.95.04.0003>.
 77. Black, L. P. et al. TEMORA 1: a new zircon standard for Phanerozoic U–Pb geochronology. *Chem. Geol.* **200**, 155–170 (2003).
 78. Ludwig, K. R. *Isoplot 3.0. A Geochronological Toolkit for Microsoft Excel*. (Berkeley Geochronology Center Special Publication, 2003).
 79. Ludwig, K. R. *SQUID II, A User's Manual*. (Berkeley Geochronology Center, Special Publication, 2009).
 80. Vermeesch, P. IsoplotR: a free and open toolbox for geochronology. *Geosci. Front.* **9**, 1479–1493 (2018).
 81. Spencer, C. J., Kirkland, C. L. & Taylor, R. J. M. Strategies towards statistically robust interpretations of in situ U–Pb zircon geochronology. *Geosci. Front.* **7**, 581–589 (2016).
 82. Wiedenbeck, M. et al. Further characterisation of the 91500 zircon crystal. *Geostand. Geoanalytical Res.* **28**, 9–39 (2004).
 83. Jackson, S. E., Pearson, N. J., Griffin, W. L. & Belousova, E. A. The application of laser ablation-inductively coupled plasma-mass spectrometry to in situ U–Pb zircon geochronology. *Chem. Geol.* **211**, 47–69 (2004).
 84. Black, L. P. et al. Improved $206\text{Pb}/238\text{U}$ microprobe geochronology by the monitoring of a trace-element-related matrix effect; SHRIMP, ID-TIMS, ELA-ICP-MS and oxygen isotope documentation for a series of zircon standards. *Chem. Geol.* **205**, 115–140 (2004).
 85. Spencer, C. J., Kirkland, C. L., Roberts, N. M. W., Evans, N. J. & Liebmann, J. Strategies towards robust interpretations of in situ zircon Lu–Hf isotope analyses. *Geosci. Front.* **11**, 843–853 (2020).
 86. Spencer, C. J. et al. Evidence for melting mud in Earth's mantle from extreme oxygen isotope signatures in zircon. *Geology* **45**, 975–978 (2017).
 87. Woodhead, J. D. & Hergt, J. M. A preliminary appraisal of seven natural zircon reference materials for in situ Hf isotope determination. *Geostand. Geoanalytical Res.* **29**, 183–195 (2005).
 88. Fisher, C. M., Vervoort, J. D. & DuFrane, S. A. Accurate Hf isotope determinations of complex zircons using the “laser ablation split stream” method. *Geochem. Geophys. Geosystems* **15**, 121–139 (2014).
 89. Morel, M. L. A., Nebel, O., Nebel-Jacobsen, Y. J., Miller, J. S. & Vroon, P. Z. Hafnium isotope characterization of the GJ-1 zircon reference material by solution and laser-ablation MC-ICPMS. *Chem. Geol.* **255**, 231–235 (2008).
 90. Paton, C., Hellstrom, J., Paul, B., Woodhead, J. & Hergt, J. Iolite: freeware for the visualisation and processing of mass spectrometric data. *J. Anal. At. Spectrom.* **26**, 2508–2518 (2011).
 91. Scherer, E., Münker, C. & Mezger, K. Calibration of the lutetium-hafnium clock. *Science* **293**, 683–687 (2001).
 92. Li, X.-H. et al. Old continental crust underlying juvenile oceanic arc: evidence from Northern Arabian-Nubian Shield, Egypt. *Geophys. Res. Lett.* **45**, 3001–3008 (2018).
 93. Yang, Q. et al. An evaluation of precision and accuracy of SIMS oxygen isotope analysis. *Solid Earth Sci.* **3**, 81–86 (2018).
 94. Li, X. H. et al. Qinghu zircon: a working reference for microbeam analysis of U–Pb age and Hf and O isotopes. *Chinese Sci. Bull.* **58**, 4647–4654 (2013).
 95. Li, X.-H. et al. Penglai zircon megacrysts: a potential new working reference material for microbeam determination of Hf–O isotopes and U–Pb. *Age. Geostand. Geoanalytical Res.* **34**, 117–134 (2010).
 96. Baertschi, P. Absolute 18O content of standard mean ocean water. *Earth Planet. Sci. Lett.* **31**, 341–344 (1976).
 97. Stern, R. J. & Hedge, C. E. Geochronologic and isotopic constraints on late Precambrian crustal evolution in the Eastern Desert of Egypt. *Am. J. Sci.* **285**, 97–127 (1985).
 98. GSE. *Geological Map of Jabal Hamatah Quadrangle, South Eastern Desert, Egypt. Scale 1: 250,000*. (Geological survey of Egypt, 1997).
 99. Peccerillo, A. & Taylor, S. R. Geochemistry of eocene calc-alkaline volcanic rocks from the Kastamonu area, Northern Turkey. *Contrib. Mineral. Petrol.* **58**, 63–81 (1976).
 100. Maniar, D. & Piccoli, M. Tectonic discrimination of granitoids. *Geol. Soc. Am. Bull.* **101**, 635–643 (1989).
 101. Georoc repository (Accessed July 2020); <http://georoc.mpch-mainz.gwdg.de/georoc/>.

Acknowledgements

We would like to thank Allen Kennedy, Hao Gao, Elaine Miller, and Brad McDonald for assisting with SHRIMP and LA-ICPMS analyses of zircon. We are greatly indebted to Dr Josh Beardmore for proofreading. Comments from Navot Morag and editor Joe Aslin helped to improve the manuscript. This work was supported by the Australian Research Council Laureate Fellowship grant to Z.-X. L. (FL150100133). Research in the John de Laeter Centre GeoHistory Facility is enabled by AuScope (auscope.org.au) and the Australian Government via the National Collaborative Research Infrastructure Strategy (NCRIS). The NPII multi-collector was obtained via funding from the Australian Research Council LIEF program (LE150100013). This is a contribution to IGCP 648: Supercontinent Cycles and Global Geodynamics.

Author contributions

H.G. and Z.-X.L. designed the project. H.G. performed the analyses, compiled the data, and drafted the manuscript. Z.-X.L. conducted the field trip with H.G. and M.A., clarified the concepts including the designing of a key figure, and assisted H.G. in the writing of the manuscript. M.A. organized the fieldwork, helped with sample collection, and commented on the manuscript. L.D. assisted with the SHRIMP analyses and edited the manuscript. J.B.M. clarified some concepts and edited the manuscript. N.E. performed the LASS analyses and edited the manuscript. X.-P.X. performed the SIMS analyses and commented on the manuscript. J.L. assisted with the SHRIMP analyses and commented on the manuscript.

Competing interests

The authors declare no competing interests.

Additional information

Supplementary information The online version contains supplementary material available at <https://doi.org/10.1038/s43247-021-00205-8>.

Correspondence and requests for materials should be addressed to H.G.E.D. or Z.-X.L.

Peer review information *Communications Earth & Environment* thanks the anonymous reviewers for their contribution to the peer review of this work. Peer reviewer reports are available. Primary handling editor: Joe Aslin.

Reprints and permission information is available at <http://www.nature.com/reprints>

Publisher's note Springer Nature remains neutral with regard to jurisdictional claims in published maps and institutional affiliations.



Open Access This article is licensed under a Creative Commons Attribution 4.0 International License, which permits use, sharing, adaptation, distribution and reproduction in any medium or format, as long as you give appropriate credit to the original author(s) and the source, provide a link to the Creative Commons license, and indicate if changes were made. The images or other third party material in this article are included in the article's Creative Commons license, unless indicated otherwise in a credit line to the material. If material is not included in the article's Creative Commons license and your intended use is not permitted by statutory regulation or exceeds the permitted use, you will need to obtain permission directly from the copyright holder. To view a copy of this license, visit <http://creativecommons.org/licenses/by/4.0/>.

© Crown 2021